HETEROCYCLES, Vol. 106, No. 8, 2023, pp.1267 - 1307. © 2023 The Japan Institute of Heterocyclic Chemistry
Received, 17th December, 2022, Accepted, 15th May, 2023, Published online, 24th May, 2023
DOI: 10.3987/REV-22-1001

1,3,5-TRIAZINE-CORED STAR-SHAPED (D–π)$_3$–A MOLECULES BASED ON 2,4,6-TRIS(5-ARYLTHIOPHEN-2-YL)-1,3,5-TRIAZINE

Hiroki Muraoka* and Satoshi Ogawa

Department of Chemistry and Biological Sciences, Faculty of Science and Engineering, Iwate University, Morioka 020-8551, Japan, muraoka@iwate-u.ac.jp

Abstract – Star-shaped (D–π)$_3$–A molecules consist of three parts: an electron-accepting core (A), π-conjugated bridges (π), and electron-donating terminals (D). These molecules are commonly designed using a π (thiophene)$_3$–A (1,3,5-triazine) segment composed of 2,4,6-tri(thiophen-2-yl)-1,3,5-triazine (**TTT**), which offers geometric and electronic structural advantages. By structurally and electronically modifying **TTT** with different types of electron-donating aryl terminals, we systematically construct **TTT**-based star-shaped (D–π)$_3$–A molecules with controlled molecular properties attributed to a special structure in which the star-shaped and D–π–A structures are hybridized. This review summarizes our researches on the synthesis, optical and electronic characterization, and application of a series of 2,4,6-tris(5-arylthiophen-2-yl)-1,3,5-triazines based on our concept.

CONTENTS

1. Introduction
2. Synthesis, characterization, and application of a series of 2,4,6-tris(5-arylthiophen-2-yl)-1,3,5-triazines (**TATTs**)
   2-1. Systematic synthesis of **TATTs**
   2-2. Optical and electronic properties of **TATTs**
   2-3. Optical sensing responses of **TATTs** to solvent polarity
   2-4. Optical sensing responses of **TATTs** to protons
   2-5. Optical sensing responses of **TATTs** to metal ions
3. Conclusion

1. INTRODUCTION

π-Conjugated molecules, characterized by a star-shaped structure formed by three or more π-conjugated side arms connected to a central core, have been actively investigated for their wide applications in material science.[1] The molecular properties (self-organization, optical, and electronic properties) originating from star-shaped geometric and electronic structures differ from those of linear π-conjugated molecules. The design of star-shaped π-conjugated molecules critically depends on the selection of the central core, because the core structure decides the number of side arms, degree of electronic interaction among the side arms through the core, and symmetry of the overall structure. 1,3,5-Triazine is an electron-deficient aza-aromatic ring with a highly symmetric structure (D_{3h}) and a strong π-conjugation effect. When used as the central core, 1,3,5-triazine creates three-branched star-shaped π-conjugated molecules with a well-defined symmetrical structure and a suitable π-conjugation length. Additionally, the 1,3,5-triazine ring functions as a strong electron-acceptor (A) owing to its high electron affinity (+0.45 eV).[2] To build star-shaped (D–π)$_3$–A molecules with a hybrid π-conjugated structure of star-shaped and D–π–A structures, the three π-conjugated side arms (π-spacers) can be end-capped with electron-donor (D) groups. Moreover, the geometric and electronic structures of 1,3,5-triazine-cored star-shaped (D–π)$_3$–A molecules can be controlled by varying the combination of terminal D and π-spacer segments, providing outstanding molecular properties (for example, formation of a supramolecular architecture through controlled self-organization, linear and nonlinear optical properties based on intramolecular charge transfer (ICT), electronic properties such as an electrical conductivity). Exploiting the diversity of molecular properties and high degree of freedom in molecular design, researchers have developed a wide variety of 1,3,5-triazine-cored star-shaped (D–π)$_3$–A molecules as functional organic materials for desired applications.[1]

2,4,6-Triphenyl-1,3,5-triazine (**TPT**) has an ideal structure with high overall symmetry and a coplanar conformation (D_{3h} symmetry) (Figure 1, left). Accordingly, **TPT** possesses an effective π-conjugation over the whole molecule and can form molecular aggregates via favorable intermolecular interactions such as π–π stacking. With its special geometrical and electronic features, **TPT** is a promising segment for the development of 1,3,5-triazine-cored star-shaped (D–π)$_3$–A molecules. Most of the 1,3,5-triazine-cored star-shaped (D–π)$_3$–A molecules have been synthesized by directly or indirectly (via π-expanded linkers) introducing electron-donating terminals to **TPT**.[3] Meanwhile, 2,4,6-tri(thiophen-2-yl)-1,3,5-triazine (**TTT**), which has a C_{3h}-symmetrical planar structure as its ideal structure (Figure 1, right), is emerging as a possible replacement of **TPT**. **TTT** offers several advantages over **TPT**. First, in each crystal structure of **TTT** and **TPT**, **TTT** takes a planar structure with almost no torsion in the **TTT** skelton,[4] whereas **TPT** takes a non-planar structure with a slight twist of the phenyl rings out of the 1,3,5-triazine plane.[5] Based on this fact, **TTT** possesses a better π-conjugation system

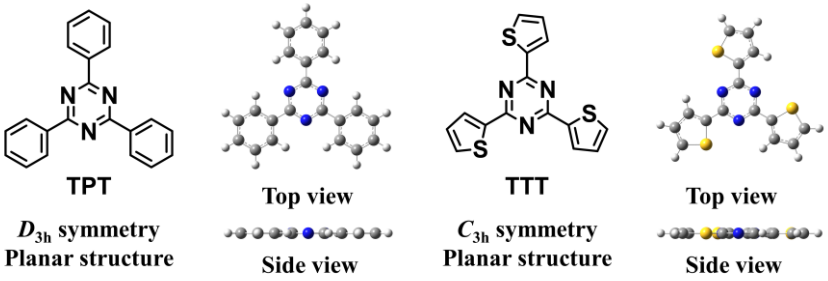

Figure 1. Chemical structures of **TPT** and **TTT** and their optimized structures calculated at the B3LYP/3-21G(d) level

than **TPT** and is more propitious as the key segment. Second, thiophene has a lower delocalization energy (lower aromatic character) and a richer π-electron density than benzene. Therefore, as a π-spacer, it induces a more effective push–pull conjugation between the electron-donor units and electron-acceptor unit within the star-shaped (D–π)$_3$–A structure. Third, as the outer α-positions of the thiophene rings in **TTT** are easily functionalized, **TTT** allows the simple design and synthesis of diverse 1,3,5-triazine-cored star-shaped (D–π)$_3$–A molecules. Motivated by these features of **TTT**, researchers have developed **TTT**-based star-shaped (D–π)$_3$–A molecules with different types of electron-donating terminals in the absence or presence of a π-expanded linker, thereby producing a new class of organic functional materials with improved optical and electronic properties for various applications.[6] The **TTT** unit is easily modified with various electron-donating aryl groups, allowing **TTT**-based star-shaped (D–π)$_3$–A molecules with controllable optical and electronic properties conferred by the geometric and electronic natures of the aryl groups. Thus, we have focused on the synthesis, characterization, and applications of 2,4,6-tris(5-arylthiophen-2-yl)-1,3,5-triazines (**TATTs**) functionalized with various kinds of electron-donating aryl terminals. This review introduces the synthesis and optical and electronic properties of our **TATT** series and the potential applications of **TATTs** in materials. Especially, **TATTs** can be employed as colorimetric and fluorometric probes for detecting environmental polarity changes and as colorimetric and fluorometric sensors for identifying specific chemical species.

2. SYNTHESIS, CHARACTERIZATION, AND APPLICATION OF A SERIES OF 2,4,6-TRIS(5-ARYLTHIOPHEN-2-YL)-1,3,5-TRIAZINES (TATTS)

2-1. Systematic synthesis of TATTs

Star-shaped (D–π)$_3$–A molecules based on **TTT** have been researched not only for elucidating their optical and electronic properties but also for verifying their potential applications as organic functional materials.[6] We have designed a family of **TTT**-based star-shaped (D–π)$_3$–A molecules with different

electron-donating aryl groups, which can be fine-tuned to improve their optical and electronic performances. Five types of *p*-substituted phenyl groups with different electron-donating substituents, namely, *n*-butyl (^{n}Bu), *n*-butoxy (^{n}BuO), di(*n*-butyl)amino (^{n}Bu$_2$N, DBA), 1-aza-15-crown 5-ether (ACE), and 2,2'-dipicolylamino (DPA), were selected as suitable electron-donating aryl groups.[7]

The **TATTs** are synthesized through the following steps: (i) The basic **TTT** skeleton is synthesized from 2,4,6-trichloro-1,3,5-triazine (**TCT**); (ii) 2,4,6-tris(5-bromothiophen-2-yl)-1,3,5-triazine (**TBTT**) is prepared by selective bromination of **TTT**; (iii) the **TATTs** are systematically synthesized via three-fold cross-coupling of **TBTT** with an aryl coupling partner. The reaction is catalyzed by a transition metal and the key intermediate **TBTT** can be partnered with many coupling reagents to produce many kinds of **TATTs**. Six **TATTs** (designated **1a–f**), including a comparative molecule without an electron-donating substituent on the benzene ring, were synthesized by this approach (see Scheme 1).

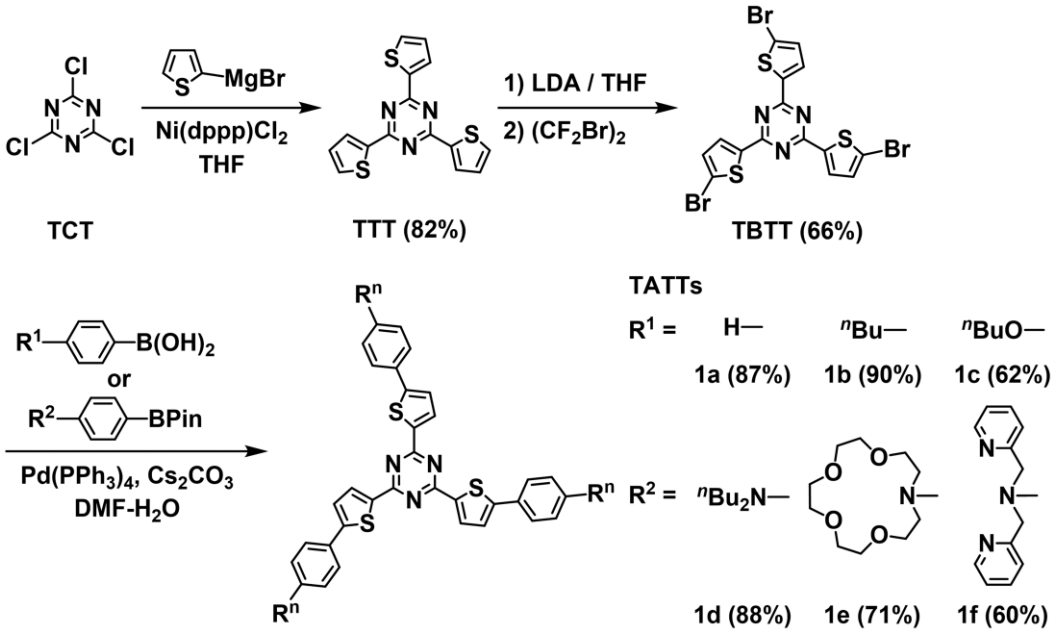

Scheme 1. Synthetic routes of **TATTs 1a–f**

When introducing three thiophen-2-yl groups into the 2-, 4-, and 6-positions of the 1,3,5-triazine ring, triple catalytic cross-coupling of **TCT** with the thienyl coupling partner is more effective than triple aromatic nucleophilic substitution of 2-metallated thiophene on **TCT**.[4] Therefore, **TTT** was first prepared in high yield (82%) via the Kumada–Tamao–Corriu cross-coupling reaction[8] between **TCT** (1 mol eq.) and thiophen-2-ylmagnesium bromide (as the thienyl coupling partner, 3.5 mol eq.) with $NiCl_2$(dppp) as the catalyst (0.05 mol eq.). In the standard methodology, the α-bromination of thiophene proceeds by α-lithiation with a lithiating agent followed by reaction with a brominating agent.[9] Based on this

methodology, **TBTT** from the above-obtained **TTT** was synthesized in good yield (66%) via selective lithiation of the 5-positions of the three thiophene rings of **TTT** (1 mol eq.) with lithium diisopropylamide (LDA, as a lithiating agent, 4.5 mol eq.), followed by bromination with 1,2-dibromo-1,1,2,2-tetrafluoroethane as the brominating agent (5 mol eq.). Finally, **TATTs 1a–f** modified with aryl groups with or without different electron-donating substituents were systematically obtained in good to high yields (60–90%) via the Suzuki–Miyaura cross-coupling reaction[10] of **TBTT** (1 mol eq.) with the corresponding aryl boronic acids and pinacol ester (as the coupling partner, 3–5 mol eq.) in the presence of Cs_2CO_3 base (6–8 mol eq.) and $Pd(PPh_3)_4$ as the catalyst (0.1–0.3 mol eq.).

2-2. Optical and electronic properties of TATTs

The optical and electronic properties of the **TATTs 1a–d** series were compared through experimental and theoretical approaches.[11]

The optical properties of **1a–d** were fully characterized using ultraviolet–visible light (UV–vis) absorption and fluorescence spectroscopies (Figure 2 and Table 1) and molecular orbital (MO) calculations (Figure 3).[7a,c]

In CH_2Cl_2 solution, the longest-wavelength absorption bands of compounds **1a**, **1b**, **1c**, and **1d** exhibited maximum-absorbance wavelengths ($\lambda_{max}^{Abs.}$) of 368, 378, 391, and 459 nm, respectively. The absorption bands were gradually redshifted and broadened with gradual increasing of the electron-donating strength of the aryl group. This result correlates with the electron-donating effect of the substituent on the benzene ring, which follows the order of $^{n}Bu_2N$ >^{n}BuO >^{n}Bu >H. From the onset wavelengths of the longest-wavelength absorption bands, the optical energy gaps between the highest occupied molecular orbital (HOMO) and the lowest unoccupied molecular orbital (LUMO) of **1a**, **1b**, **1c**, and **1d** were calculated as $E_g^{Opt.}$ = 3.08, 2.98, 2.86, and 2.43 eV, respectively. The tendency of $E_g^{Opt.}$ is consistent with the expected reduction of the HOMO–LUMO energy gap caused by the electron-donating ability of the aryl terminals, reflecting the strengthening of the inductive and resonance electron-donating effects of the substituent on the benzene ring.

The MO calculations reveal almost identical orbital shapes (HOMO and doubly degenerated LUMO, respectively) in the C_3-symmetrical real model **1a** and the C_3-symmetrical short-chain models **1b′**, **1c′**, and **1d′** with methyl (Me), methoxy (MeO), and dimethylamino (Me_2N) groups on the benzene rings, respectively. That is, the HOMO and LUMO are mainly located on the three peripheral arylthienyl moieties and the trithienyltriazine moieties, respectively. Judging from the partial overlap between the

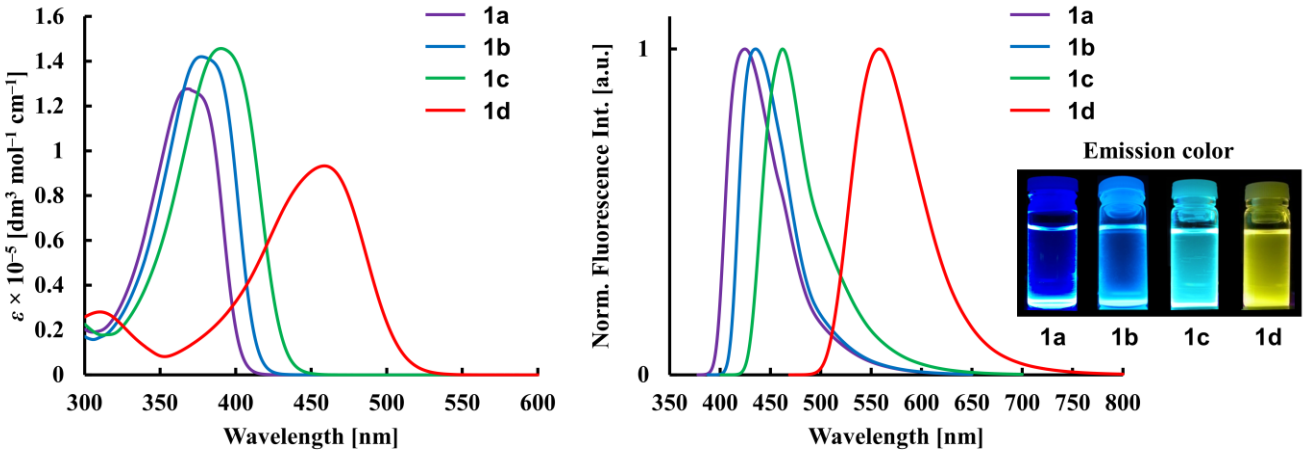

Figure 2. UV–vis absorption (left) and normalized fluorescence (right) spectra of **1a–d** in CH_2Cl_2 solution. Inset: photographs of **1a–d** in CH_2Cl_2 solution under UV light (365 nm).

Table 1. Optical data of **1a–d** in the solution state

TATT	$\lambda_{max}^{Abs.a}$ [nm]	$\varepsilon \times 10^{-5}$ [$dm^3\ mol^{-1}\ cm^{-1}$]	$E_g^{Opt.b}$ [eV]	$\lambda_{max}^{Flu.c}$ [nm]	$\Phi^{c,d}$ [–]	Stokes shift [nm (cm^{-1})]
1a	368	1.28	3.08	424	0.12	56 (3,589)
1b	378	1.42	2.98	436	0.16	58 (3,519)
1c	391	1.46	2.86	462	0.16	71 (3,930)
1d	459	0.93	2.43	558	0.10	99 (3,865)

[a]Measured for a 10 μmol dm^{-3} sample in CH_2Cl_2 solution. [b]Calculated as $E_g^{Opt.} = 1240/\lambda_{onset}^{Abs.}$, where $\lambda_{onset}^{Abs.}$ is the onset point of the longest-wavelength absorption edge. [c]Measured for a 50 μmol dm^{-3} sample in CH_2Cl_2 solution. Excitation at maximum absorption wavelength ($\lambda_{max}^{Abs.}$). [d]Absolute fluorescence quantum yield determined by a calibrated integrating sphere system.

HOMO and LUMO on the thiophene moieties, the lowest-energy electronic transition from the HOMO to the LUMO corresponds to the π–π^* transition, which triggers the ICT process from the three electron-donating aryl terminals (π) to the 1,3,5-triazine acceptor core (π^*) through the thiophene π-spacer (which acts as an effective π-conjugated transmitter in the ICT). Thus, the observed absorption bands of **1a–d** can be assigned to π–π^*-type ICT transitions, including two electronic transitions from the HOMO to the doubly degenerated LUMO. It should be noted that even phenyl groups without an electron-donating substituent behave as electron-donating aryl terminals because the 1,3,5-triazine core is a strong electron acceptor. Furthermore, as the electron-donating strength of the aryl group increases, both the HOMO and LUMO are gradually destabilized and the HOMO–LUMO energy gap gradually narrows because the HOMO destabilizes more strongly than the LUMO. The electronic transition energies from

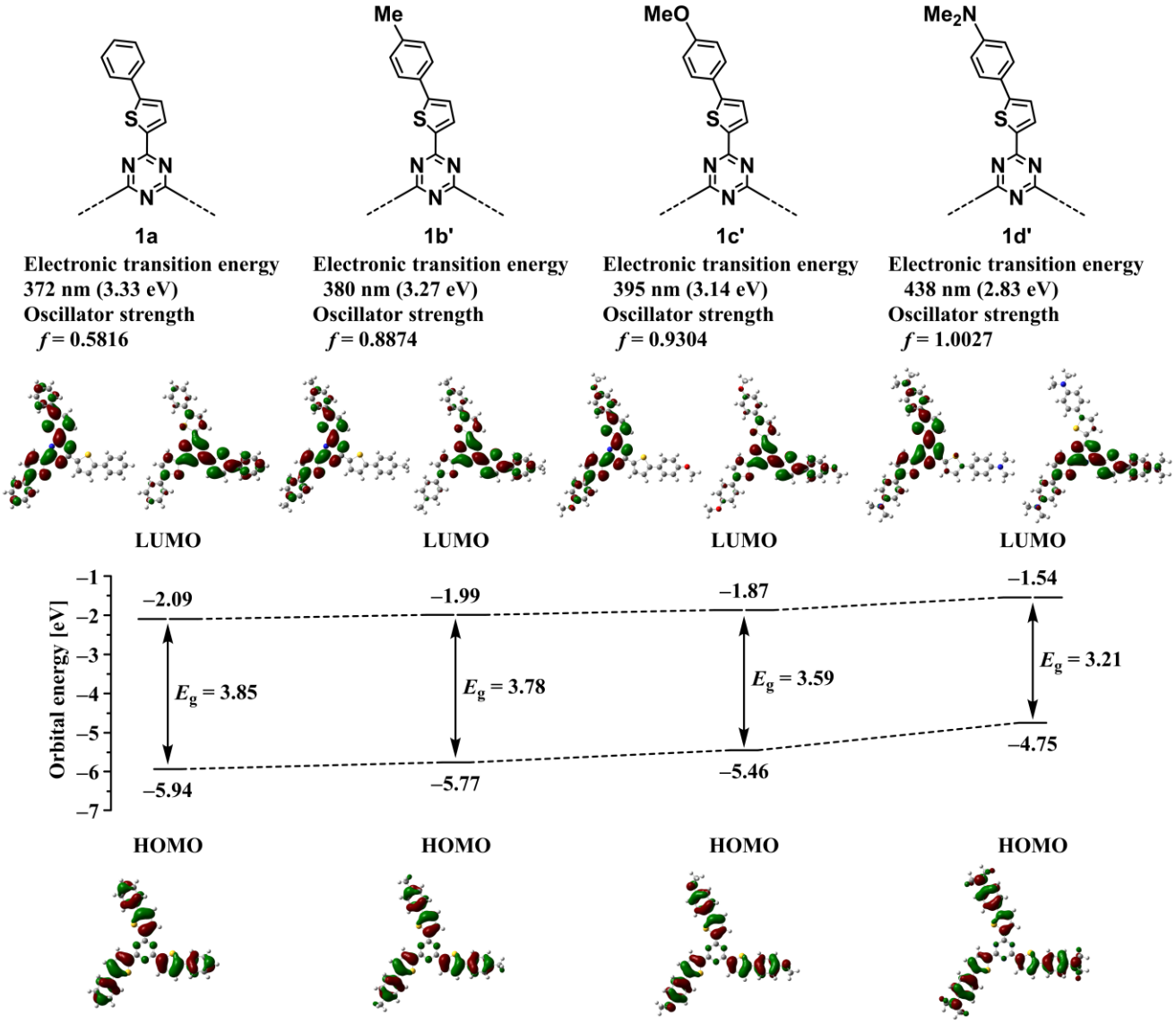

Figure 3. Molecular orbital energy diagrams and isodensity surface plots of **1a** and **1b′–d′** optimized at the B3LYP/3-21G(d) level. Also shown are the electronic transition energies and oscillator strengths calculated at the time-dependent (TD)-B3LYP/6-31G(d,p) level for each optimized structure.

the HOMO to the LUMO in **1a**, **1b′**, **1c′**, and **1d′**, which correspond to the theoretically predicted $\lambda_{max}^{Abs.}$ values, were determined as 372, 380, 395, and 438 nm, respectively, corroborating the experimentally observed $\lambda_{max}^{Abs.}$ redshifts from **1a** to **1d**. The absorption spectral feature of **1d** was broader and more redshifted than those of **1a–c**, clearly indicating a greater contribution of the ICT nature of the π–π* transition in **1d** than in the other compounds.

In CH_2Cl_2 solution, compounds **1a**, **1b**, **1c**, and **1d** exhibited fluorescence bands with maximum fluorescence wavelengths ($\lambda_{max}^{Flu.}$) of 424, 436, 462 and 558 nm, respectively, at quantum yields (Φ) of

0.12, 0.16, 0.16 and 0.10, respectively. Reflecting the differences among their $\lambda_{max}^{Flu.}$ values, the compounds emitted at different colors: blue (**1a** and **1b**), sky-blue (**1c**), or yellow (**1d**). The fluorescence bands were gradually redshifted with increasing electron-donating strength of the aryl group, as observed for the absorption bands. The moderate Stokes shift (3,500–4,000 cm^{-1}) indicates moderate geometric and electronic structural changes in the excited state, which result from the enhanced push–pull conjugation effect of the photoinduced ICT process. In other words, compounds **1a–d** with nearly planar structures in the ground state became more planar in the excited state, meaning that they emit in the planar ICT excited state. Compounds **1c–d** are more structurally planar in the ground state because the lone electron pair on the alkoxy-oxygen or amino-nitrogen atom exerts an electron-donating resonance effect. The degree of structural change of **1c–d** between the ground and excited states is reduced and the Stokes shift is reduced accordingly. Nevertheless, **1c–d** exhibited a slightly larger Stokes shift than **1a–b**. This fact clarifies that the ICT excited states of **1c–d** (which possess more powerful electron-donating substituents than **1a–b**) establish a more polar structure than those in **1a–b**. Therefore, the ICT excited states of **1c-d** are effectively stabilized by the solvation shell of CH_2Cl_2, which (as a moderately polar solvent) enlarges the Stokes shift. The electron-donating substituents on the benzene rings favor the ICT-induced enhancement of push–pull conjugation as the single bonds connecting the benzene, thiophene, and 1,3,5-triazine units gain a stronger double-bond character in the excited state than in the ground state. Strengthening the double-bond character suppresses the molecular motions, enabling thermal deactivation of the excited state through a nonradiative process.[12] Therefore, the larger Φ values of **1b–c** than of **1a** can be interpreted as a decrease of unfavorable excited-state motions. Increasing the electron-donating effect of the substituent on the benzene ring increases the structural rigidity of the ICT excited state and hence the fluorescence efficiency. Although the ICT excited state of **1d** is more structurally rigid than the other compounds owing to the strong electron-donating resonance effect of the amino-nitrogen atom, **1d** obtained the lowest Φ among the compounds. This observation can be explained by the high structural polarity of the ICT excited state. This polarized excited state strongly interacts with the polar solvent molecules, promoting the nonradiative decay process and lowering the fluorescence efficiency.[13] Judging from the larger Stokes shift and lower fluorescence quantum yield of **1d** than of the other compounds, the contribution of the ICT nature is stronger in the emissive excited state of **1d** than in the emissive excited states of the other compounds, as supported by the broadened fluorescence spectral feature of **1d**.

After comparing the optical properties of **1a–d** with four kinds of aryl terminals with or without different electron-donating substituents, we concluded that the absorption and fluorescence wavelengths, Stokes shift, and fluorescence quantum yield of **TATTs** can be fine-tuned by the degree of ICT, which is itself controlled by the electron-donating strength of the aryl terminals.

The electron-donating and electron-accepting capacities of D–π–A molecules can be determined by cyclic voltammetry (CV), which utilizes the electrochemical oxidation and reduction reactions. Figure 4 and Table 2 show the results of CV experiments on **1a–d**, from which the electrochemical redox behavior of the **TATTs** was determined.[7a]

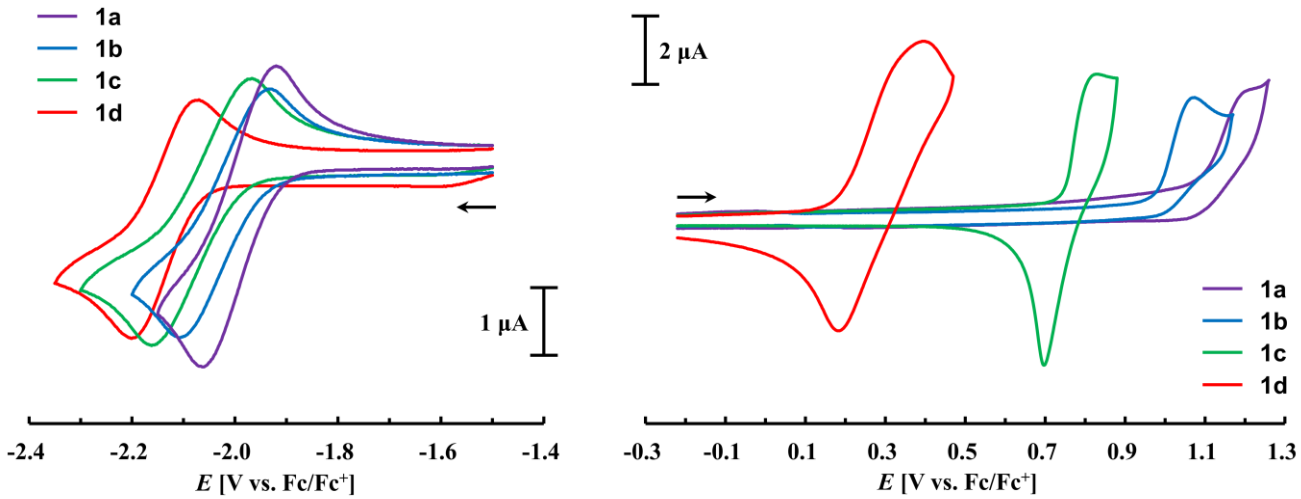

Figure 4. Cyclic voltammograms of **1a–d** in a 0.1 mol dm^{-3} solution of [Bu_4N][PF_6] in THF (negative scan, left) and in CH_2Cl_2 solution (positive scan, right)

Table 2. Electrochemical data of **1a–d**

TATT	$E_{pa}^{Ox.a}$ [V]	$E_{pc}^{Ox.a}$ [V]	$E_{1/2}^{Ox.a}$ [V]	$E_{HOMO}^{Elec.b}$ [eV]	$E_{pa}^{Red.a}$ [V]	$E_{pc}^{Red.a}$ [V]	$E_{1/2}^{Red.a}$ [V]	$E_{LUMO}^{Elec.b}$ [eV]	$E_g^{Elec.c}$ [V]
1a	+1.22[d]	–[d]	–[d]	–5.90	–1.92	–2.06	–1.99	–2.89	3.01
1b	+1.07[d]	–[d]	–[d]	–5.77	–1.94	–2.09	–2.02	–2.86	2.91
1c	+0.82[e]	+0.70[e]	–[e]	–5.55	–1.98	–2.15	–2.07	–2.81	2.74
1d	+0.39	+0.19	+0.29	–4.99	–2.08	–2.19	–2.14	–2.73	2.26

[a]Measured for a 1.0 mmol dm^{-3} sample in 0.1 mol dm^{-3} [Bu_4N][PF_6]/CH_2Cl_2 solution (positive scan) and a 1.0 mmol dm^{-3} sample in 0.1 mol dm^{-3} [Bu_4N][PF_6]/THF solution (negative scan) using glassy carbon as the working electrode, Ag/Ag^+ (0.01 mol dm^{-3} $AgNO_3$ in 0.1 mol dm^{-3} [Bu_4N][PF_6]/MeCN solution) as the reference electrode, and a Pt counter-electrode. The scan rate was 200 mV s^{-1}. The potentials were externally calibrated using the ferrocene/ferrocenium (Fc/Fc^+) redox couple (4.8 eV below the vacuum level). The anodic peak (E_{pa}), cathodic peak (E_{pc}) and half-wave [$E_{1/2}$ = 0.5(E_{pa} + E_{pc})] potentials vs. Fc/Fc^+ were determined for each oxidation (Ox.) and reduction (Red.) process. [b]Calculated as $E_{HOMO}^{Elec.} = -e(4.8 + E_{pa,\,onset}^{Ox.})$ and $E_{LUMO}^{Elec.} = -e(4.8 + E_{pc,\,onset}^{Red.})$, where e is the elementary charge, $E_{pa,\,onset}^{Ox.}$ is the oxidation onset potential, and $E_{pc,\,onset}^{Red.}$ is the reduction onset potential. [c]Calculated as $E_g^{Elec.} = E_{LUMO}^{Elec.} - E_{HOMO}^{Elec.}$. [d]Irreversible oxidation process. [e]Quasi-reversible oxidation process.

Over the positive scan, compounds **1a**, **1b**, **1c**, and **1d** each showed a single oxidation wave with an anodic peak potential ($E_{pa}^{Ox.}$) at +1.22, +1.07, +0.82 and +0.39 V vs. ferrocene/ferrocenium (Fc/Fc^{+}), respectively. However, the electrochemical reaction was irreversible for **1a** and **1b**, quasi-reversible for **1c**, and reversible for **1d**. This observation clarifies that enhancing the electron-donating strength of the aryl group enhances both the electron-donating ability (evidenced by a shift of the oxidation potential to lower energy) and stability of the cation state generated by the oxidation reaction (evidenced by enhancement of the electrochemical reversibility). Compound **1d**, having amino substituents with the highest electron-donating capacity, is the most easily oxidized and forms the most stable cation state among the **TATT** compounds. Given that the HOMO of the model compound **1d′** is distributed over the three peripheral π-conjugated side arms containing the amino substituents on the benzene rings, the oxidation reaction of **1d** was inferred to occur on the electron-donating amino-nitrogen atoms. Accordingly, the electrochemical oxidation of **1d** can be assigned to the formation of the tri(radical cation) state with three aminium radical cation centers derived from a one-step three-electron oxidation (three overlapping one-electron oxidations) of the three independent amino-donor terminals. The special stability of the tri(radical cation) of **1d** is mainly attributable to stabilization of the aminium radical cation center within each π-conjugated side arm linked to the 1,3,5-triazine core. Here, stabilization is achieved by the spin-delocalization effect of the benzene ring bound to the radical centers. In other words, the benzenoid-to-quinoid transformation of the benzene ring effectively delocalizes the unpaired electron on the nitrogen atom across the π-conjugated side arm. The three amono centers are simultaneously oxidized at the same potential because no electronic communication (electron delocalization) occurs between the aminium radical cation center and the neutral amino center in the partially oxidized (mixed-valent) state. Therefore, the 1,3,5-triazine core might block electron delocalization between the aminium and amino centers on the π-conjugated side arms.[14]

Over the negative scan, compounds **1a**, **1b**, **1c**, and **1d** each showed a single reduction wave with a cathodic peak potential ($E_{pc}^{Red.}$) at –2.06, –2.09, –2.15, and –2.19 V vs. Fc/Fc^{+}, respectively. As the electron-donating strength of the aryl group increased, the reduction potential shifted to higher energy. The electrochemical reduction process of **1a–d** can be assigned to the formation of a radical anion derived from one-electron reduction of the 1,3,5-triazine core. Corroborating this assignment, the doubly degenerated LUMO in the **1a** and **1b′–d′** models is predominantly centered on the 1,3,5-triazine core. Reversible one-electron transfer between the neutral and radical anion states occurs independently of the electron-donating aryl terminals because the radical anions of **1a–d** are stabilized by the high electron deficiency of the 1,3,5-triazine core.

Assuming that the energy level of Fc/Fc^+ is 4.8 V below the vacuum level, the HOMO and LUMO energy levels ($E_{HOMO}^{Elec.}$ and $E_{LUMO}^{Elec.}$, respectively) can be experimentally calculated from the onset oxidation $E_{pa,\ onset}^{Ox.}$ and the onset reduction potential $E_{pc,\ onset}^{Red.}$, respectively,[15]

$$E_{HOMO}^{Elec.} = -IP = -e(4.8 + E_{pa,\ onset}^{Ox.})\ [eV],$$

$$E_{LUMO}^{Elec.} = -EA = -e(4.8 + E_{pc,\ onset}^{Red.})\ [eV],$$

where IP is the ionization potential, EA is the electron affinity, and e is the elementary charge. The $E_{HOMO}^{Elec.}$ levels of **1a**, **1b**, **1c**, and **1d** were obtained as –5.90, –5.77, –5.55, and –4.99 eV, respectively, and the $E_{LUMO}^{Elec.}$ levels of them were obtained as –2.89, –2.86, –2.81, and –2.73 eV, respectively. The electrochemical HOMO–LUMO energy gaps ($E_g^{Elec.}$) of **1a**, **1b**, **1c**, and **1d** were then calculated as the differences between the $E_{HOMO}^{Elec.}$ and $E_{LUMO}^{Elec.}$ levels, obtaining 3.01, 2.91, 2.74, and 2.26 eV, respectively. The variation trends of the energy levels of $E_{HOMO}^{Elec.}$ and $E_{LUMO}^{Elec.}$ and their energy gaps ($E_g^{Elec.}$) experimentally demonstrate that when the electron-donating effect of the substituent on the benzene ring increases, the HOMO energy level is destabilized to a much greater extent than the LUMO energy level; consequently, the HOMO–LUMO energy gap reduces. The $E_g^{Elec.}$ values well agree with the optical values ($E_g^{Opt.}$) determined from the onset points of the longest-wavelength absorption edges, corroborating that **TATT** becomes a longer-wavelength absorber as the electron-donating ability of its aryl group increases.

These findings reveal that **TATTs** possess electron-donating and electron-accepting capacities contributed by their coexisting electron acceptor (1,3,5-triazine core) and electron donors (aryl terminals) within a single molecule. Therefore, **TATTs** undergo both electrochemical oxidation and reduction processes. It is worth noting that the electrochemical oxidation performance (potential and reversibility) of a **TATT** can be controlled by manipulating the electron-donating ability of its aryl group.

To investigate the structural and optical properties of **1c–d** in the film state, thin films of these compounds were prepared via thermal vacuum deposition. The feasibilities of the thin films as active layers in organic field-effect transistors (OFETs) were investigated.[16]

First, the structures of the **1c–d** thin films vacuum-deposited on a quartz substrate were characterized by X-ray diffraction (XRD) analysis. The out-of-plane XRD patterns in the total reflection region of both films revealed periodic intensity oscillations (Kiessig oscillations), suggesting smooth film surfaces. From the periodicity of the oscillations, the thicknesses of the **1c** and **1d** films were estimated as 114 and 86.5 nm, respectively. Beyond the total reflection region, the films showed no clear diffraction peaks,

only a very broad peak originating from the substrate, clarifying that both compounds formed an amorphous structure in the vacuum-deposited films.

Second, the optical properties of the **1c–d** thin films were identified by UV–vis absorption and fluorescence spectroscopies (Table 3).

Table 3. Optical data of **1c–d** in the thin-film state

TATT	Film thickness [nm]	$\lambda_{max}^{Abs.a}$ [nm]	$E_g^{Opt.b}$ [eV]	$\lambda_{max}^{Flu.a}$ [nm]	Stokes shift [nm (cm^{-1})]
1c	114	388	2.78	489	101 (5,323)
1d	86.5	447	2.38	574	127 (4,949)

[a]Measured in a thin film deposited on a quartz substrate. Excitation at maximum absorption wavelength ($\lambda_{max}^{Abs.}$). [b]Calculated as $E_g^{Opt.} = 1240/\lambda_{onset}^{Abs.}$, where $\lambda_{onset}^{Abs.}$ is the onset point of the longest-wavelength absorption edge.

When the solution state (in CH_2Cl_2) changed to the film state, the absorption maxima of the longest-wavelength absorption bands ($\lambda_{max}^{Abs.}$) of **1c** and **1d** were slightly blue-shifted from 391 to 388 nm ($\Delta\lambda_{max}^{Abs.}$ = 3 nm) and from 459 to 447 nm ($\Delta\lambda_{max}^{Abs.}$ = 12 nm), respectively. In contrast, the fluorescence maxima ($\lambda_{max}^{Flu.}$) of **1c** and **1d** were slightly redshifted from 462 to 489 nm ($\Delta\lambda_{max}^{Flu.}$ = 27 nm) and from 558 to 574 nm ($\Delta\lambda_{max}^{Flu.}$ = 16 nm), respectively. The films of **1c** and **1d** emitted green and orange light, respectively. Consequent to the slightly blue-shifted $\lambda_{max}^{Abs.}$ and redshifted $\lambda_{max}^{Flu.}$ in the film state compared to the solution state, the Stokes shift slightly increased from 71 nm (3,930 cm^{-1}) to 101 nm (5,323 cm^{-1}) in the **1c** film and from 99 nm (3,865 cm^{-1}) to 127 nm (4,949 cm^{-1}) in the **1d** film. The optical HOMO–LUMO energy gaps ($E_g^{Opt.}$) of the **1c** and **1d** films were estimated as 2.78 and 2.38 eV, respectively, similar to those in the solution state ($E_g^{Opt.}$ = 2.86 eV for **1c** and 2.43 eV for **1d**). As the optical properties of both **1c** and **1d** were very similar in the solution and film states, the intermolecular electronic interactions in the **1c–d** films were concluded to be extremely weak due to the amorphous film structures. The small differences between the optical properties of the solution and film states were attributed to different conformations and/or dielectric environments in the two states.

Films of **1c–d** (nominal thickness = 50 nm) were prepared as the active layers of SiO_2/Si wafers in top-contact OFET devices employing Au source/drain electrodes. The device containing **1d** showed only *p*-type OFET characteristics with a threshold voltage (V_{th}) of 7.6 V, a drain-source current (I_{DS}) of 4.6×10^{-6} A with a drain-source voltage (V_{GS}) of –20 V, and a hole carrier mobility (μ_h) of 2×10^{-6} $cm^2\,V^{-1}\,s^{-1}$.

The selective carrier transport and low mobility of the **1d** film can be explained in terms of the electronic structure and film structure. The HOMO and LUMO energy levels of the compounds were determined from the CV data of **1c–d** and the MO calculations of **1c′–d′**. The HOMO was much closer to the work function (Fermi level) of Au than the LUMO, indicating that hole injection from the Au electrode was easier than electron injection. Moreover, owing to the lower hole-injection barrier, hole injection was more effective in the **1d** film than in the **1c** film. Judging from the HOMO and LUMO distributions in **1c′–d′**, hole or electron transport in the **1c–d** films requires the orbital overlap of the aryl–thienyl moieties (the main sites of the HOMO) or the orbital overlap of the 1,3,5-triazine core (the main site of the LUMO). As the aryl–thienyl moieties occupy a much higher volume than the 1,3,5-triazine core in the film, they are more favorably overlapped than the 1,3,5-triazine core; accordingly, hole transport is more efficient than electron transport. The μ_h is also lowered by the small overlap degree of the aryl–thienyl moieties owing to the amorphous structure of the film.

The structural, optical and electrical characterization of the **1c–d** thin films revealed that **TATT** films tend to form an amorphous structure and their inherent optical and electrical conductive properties depend on the electron-donating aryl groups.

2-3. Optical sensing responses of TATTs to solvent polarity

Two important features of D–*π*–A molecules are solvatochromism and fluorosolvatochromism, referring to the changes in solution and emission colors, respectively, induced by spectral shifts in light absorption and fluorescence as the solvent polarity changes. The photoinduced ICT process, which changes the polarity (dipole moment) between the electronic ground and excited states, plays an important role in solvatochromic behavior and sensitivity. Therefore, the solvatochromic response of D–*π*–A molecules can be easily and desirably tuned by modifying the D/*π*-spacer/A couple and hence modulating the degree of ICT. Based on this concept, a solvatochromic chromophore and fluorophore based on the D–*π*–A structural system was integrated into a colorimetric and fluorometric probe with a color response to solvent polarity.[17] For this purpose, **TATTs 1d–f** possessing strong amino-electron-donating groups within the $(D–\pi)_3–A$ system were selected for their strong ICT nature. The solvatochromic behavior of **1d–f** was determined from their UV–vis absorption and fluorescence spectra in various organic solvents with different polarities.[7]

The optical spectral responses of **1d** [with di(*n*-butyl)amino (DBA) groups] in solvents with different polarities are compared in Figure 5 and the corresponding data are listed in Table 4.

The solvent polarity is correlated with relative permittivity. As the polarity increased from non-polar (*n*-hexane) to polar (DMF), the absorption maximum of the longest-wavelength absorption band ($\lambda_{max}^{Abs.}$) was slightly redshifted by 26 nm (from 442 to 468 nm); accordingly, the solution color changed from yellowish-green to orange. The weak positive solvatochromic shift clarifies that in a polar solvent, the Franck–Condon (FC) excited state is more stabilized than the ground state due to its slightly higher dipole moment, thereby reducing the absorption transition energy. To explain the above finding, we note that the dipole moment of the FC excited state increases with increasing contribution of the polarized (charge-separated) resonance structure, owing to the push–pull resonance effect between the electron-pushing (electron-donating) amino-nitrogen atom and the electron-pulling (electron-accepting) imino-nitrogen atom within the 1,3,5-triazine core across the π-bonds of the benzene and thiophene rings.

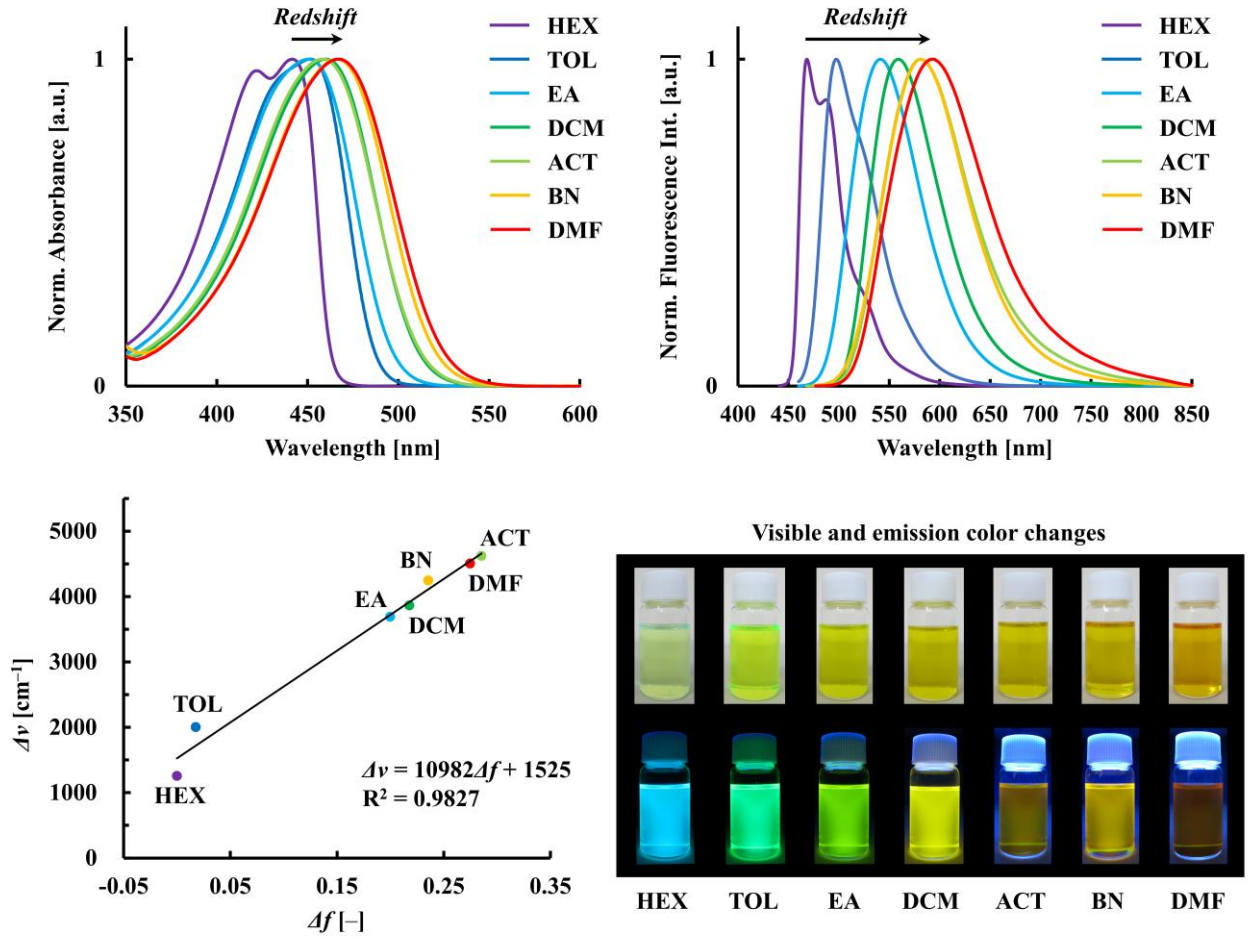

Figure 5. UV–vis absorption spectra (top left) and normalized fluorescence spectra (top right) of **1d** in various solutions. Lippert–Mataga plots of $\Delta\nu$ [cm^{-1}] vs. Δf [–] for **1d** in solvents of different polarities (bottom left). Photographs of **1d** in various solutions under room light and UV light (365 nm) (bottom right). HEX, TOL, EA, DCM, ACT, BN, and DMF represent *n*-hexane, toluene, ethyl acetate, dichloromethane, acetone, benzonitrile, and *N*,*N*-dimethylformamide, respectively.

Table 4. Optical data of **1d** in various solutions

Solvent[a]	$\lambda_{max}^{Abs.b}$ [nm]	$\varepsilon \times 10^{-5}$ [$dm^3\ mol^{-1}\ cm^{-1}$]	$\lambda_{max}^{Flu.c}$ [nm]	$\Phi^{c,d}$ [–]	Stokes shift [nm (cm^{-1})]
HEX	442	0.98	468	0.53	26 (1,256)
TOL	452	1.11	497	0.69	45 (2,003)
EA	451	1.03	541	0.24	90 (3,689)
DCM	459	0.93	558	0.10	99 (3,865)
ACT	458	0.94	581	< 0.01	123 (4,622)
BN	466	1.02	581	0.02	115 (4,247)
DMF	468	0.91	593	< 0.01	125 (4,505)

[a]Relative permittivities (ε_r): *n*-hexane (HEX) = 1.89; toluene (TOL) = 2.43; ethyl acetate (EA) = 6.03; dichloromethane (DCM) = 9.02; acetone (ACT) = 21.36; benzonitrile (BN) = 25.30; *N*,*N*-dimethylformamide (DMF) = 37.06. [b]Measured for a 10 μmol dm^{-3} sample in each solution. [c]Measured for a 50 μmol dm^{-3} sample in each solution. Excitation at maximum absorption wavelength ($\lambda_{max}^{Abs.}$). [d]Absolute fluorescence quantum yield determined by a calibrated integrating sphere system.

In contrast, the fluorescence maximum ($\lambda_{max}^{Flu.}$) was largely redshifted by 125 nm (from 468 nm to 593 nm) while the Stokes shift increased and the quantum yield (Φ) decreased; consequently, the emission color changed from blue to orange. The strong positive fluorosolvatochromic shift is attributable to the formation of a polar-solvent-stabilized ICT-excited state (that is, a thermally equilibrated emissive excited state) through the following vibrational and solvent relaxation processes: (i) The FC excited state conformationally relaxes to the lower-energy ICT excited state with a stronger polarized resonance structure (i.e., a much larger dipole moment); (ii) the surrounding polar-solvent molecules rotationally reorient to stabilize the dipole moment of the ICT excited state through dipole–dipole solute–solvent interactions. This reorientation further lowers the energy level of the ICT excited state and hence reduces the emission transition energy in a more polar solvent.

The solvent polarity largely affects the fluorescence properties of **1d**, implying that the highly polarized structure of the ICT excited state imposes a large dipole moment on that state. To quantify the dipole moment of the excited state of **1d**, we determined the dependence of the Stokes shift ($\Delta\nu = \nu_{Abs.} - \nu_{Flu.}$) on the solvent polarity parameter (Δf) using the Lippert–Mataga equation:[18]

$$\nu_{Abs} - \nu_{Flu} = \frac{2(\mu_e - \mu_g)^2}{4\pi\varepsilon_0 hca^3}\left(\frac{\varepsilon - 1}{2\varepsilon + 1} - \frac{n^2 - 1}{2n^2 + 1}\right) + \text{constant},$$

$$\Delta\nu = \frac{2\Delta\mu^2}{4\pi\varepsilon_0 hca^3}\Delta f + \text{constant},$$

where $\Delta\mu = \mu_e - \mu_g$ is the difference between the dipole moments of the excited and ground states, ε_0 is the permittivity in a vacuum, h is Planck's constant, c is the speed of light, a is the Onsager cavity radius, and ε and n are the relative permittivity and refractive index of the solvent, respectively. The Onsager cavity radius of **1d** is the approximate molecular radius, defined as the average distance between the three amino-nitrogen atoms (electron-donor centers) and the center of the 1,3,5-triazine core (electron-acceptor center). In the optimized structure of **1d′**, this value was determined as 10.7 Å. Linear regression of the Lippert–Mataga plot yielded a slope of 10,982 cm^{-1} (Figure 5). Inserting the obtained slope and the molecular radius into the Lippert–Mataga equation, $\Delta\mu$ was calculated as 36.6 D. Setting μ_g = 0.2 D in the optimized structure of **1d′**, μ_e was then calculated as 36.8 D. This result clarifies that the fluorosolvatochromism of **1d** originates from the excited state with a large dipole moment, namely, the strongly polarized ICT excited state. In the ground state, the dipole moment of **1d** almost vanishes owing to the C_3-symmetrical structure, as corroborated by the very small μ_g of **1d′**. In contrast, the high dipole moment of the excited state is rationalized not only by the high degree of charge transfer from the electron-donating terminals (ICT donors) to the electron-accepting core (ICT acceptor) through the π-spacer but also by breakup of the C_3-symmetrical structure in the excited state, inducing a localized ICT process. This process implies that only one or two of the three ICT donors approaches the ICT acceptor to form a partial ICT structure (a partially polarized resonance structure).[19]

To elucidate the solvatochromic responses of **1e–f** with different amino-electron-donating groups (such as ACE and DPA), the effects of solvent polarity on the UV–vis absorption and fluorescence spectra of **1e–f** were revealed in solvents with different polarities (Figure 6 and Table 5).

As the solvent polarity increased from non-polar (1,4-dioxane) to polar (DMF), both compounds exhibited a weak positive solvatochromism with a slight redshift of the longest-wavelength absorption band along with an increase in bandwidth. The solvatochromism of each compound was confirmed by the solution color, which changed from yellowish-green to yellow to yellowish-orange. As the polarity increased from non-polar to polar, the absorption maximum $\lambda_{max}^{Abs.}$ redshifted by 15 nm, indicating that the FC excited state became increasingly more stabilized, with consequent decrease in the absorption transition energy (manifesting as a wavelength increase of the absorbed light). This trend can be explained by the ICT between the electron-donating amino terminals and the electron-accepting 1,3,5-triazine core across the π-conjugated phenylene–thiophenylene linkers, which increases the charge

distribution during electronic transitions from the ground state to the FC excited state.

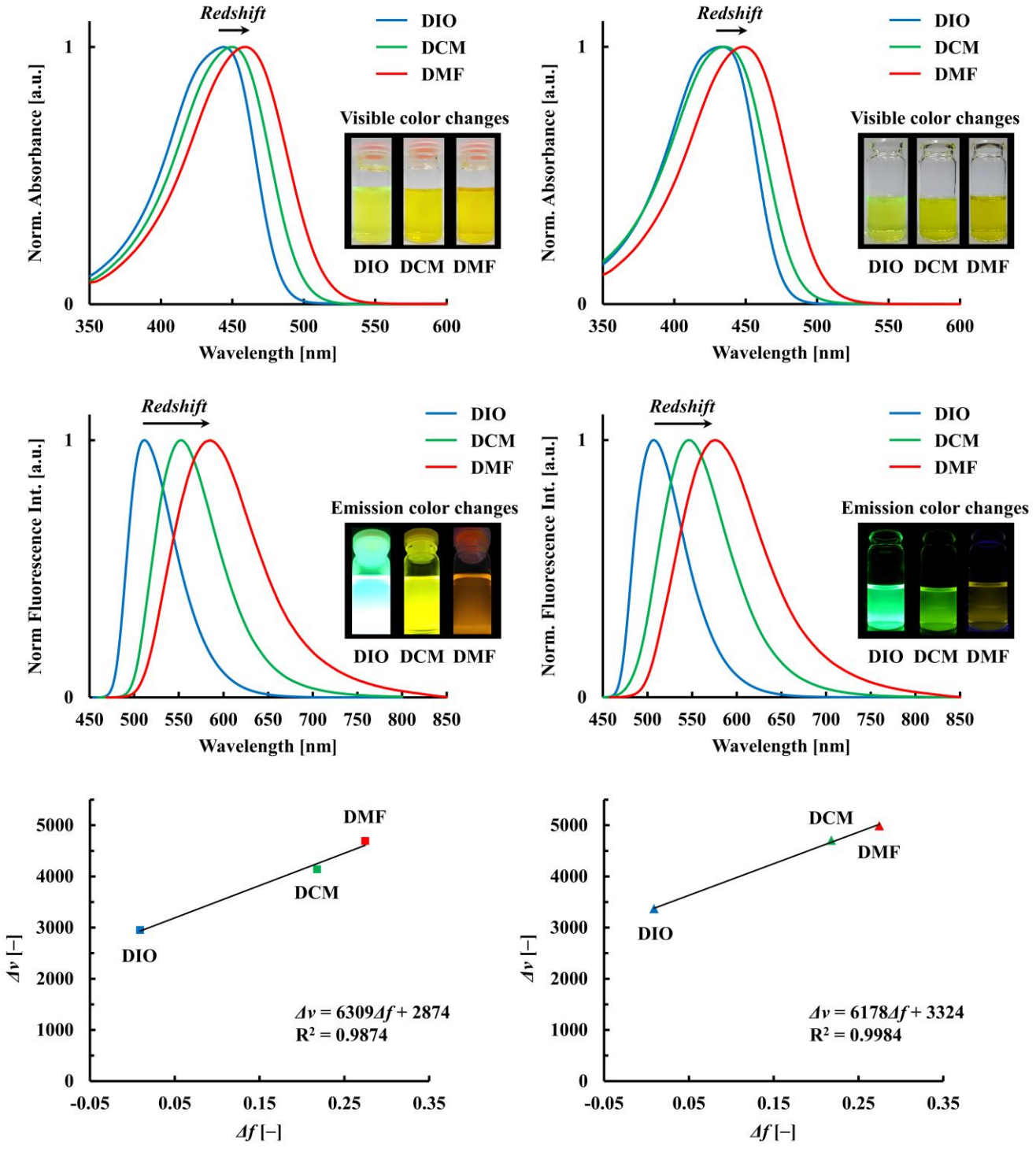

Figure 6. Solvatochromic and fluorosolvatochromic properties of **1e** (left) and **1f** (right). UV–vis absorption (top) and normalized fluorescence (middle) spectra in various solutions. Lippert–Mataga plots of $\Delta\nu$ [cm^{-1}] vs. Δf [–] in solvents with different polarities (bottom). Inset: photographs of **1e–f** in various solutions under room light and UV light (365 nm). DIO, DCM, and DMF represent 1,4-dioxane, dichloromethane, and *N*,*N*-dimethylformamide, respectively.

Table 5. Optical data of **1e–f** in various solvents

TATT	Solvent[a]	$\lambda_{max}^{Abs.b}$ [nm]	$\varepsilon \times 10^{-5}$ [$dm^3\ mol^{-1}\ cm^{-1}$]	$\lambda_{max}^{Flu.c}$ [nm]	$\Phi^{c,d}$ [–]	Stokes shift [nm (cm^{-1})]
1e	DIO	444	1.10	511	0.61	67 (2,954)
	DCM	450	1.05	553	0.08	103 (4,139)
	DMF	459	0.89	585	< 0.01	126 (4,692)
1f	DIO	433	1.11	507	0.51	74 (3,371)
	DCM	435	1.00	547	0.05	112 (4,707)
	DMF	448	0.76	577	< 0.01	129 (4,990)

[a]Relative permittivities (ε_r): 1,4-dioxane (DIO) = 2.102; dichloromethane (DCM) = 9.02; *N*,*N*-dimethylformamide (DMF) = 37.06. [b]Measured for a 10 μmol dm^{-3} sample in each solution. [c]Measured for a 50 μmol dm^{-3} sample in each solution. Excitation at maximum absorption wavelength ($\lambda_{max}^{Abs.}$). [d]Absolute fluorescence quantum yield determined by a calibrated integrating sphere system.

As demonstrated in the MO calculations[11] of the C_3-symmetrical real models of **1e–f** with the ACE and DPA groups (Figure 7), the distributions of the HOMO and doubly degenerated LUMO are very similar to those in **1d′**, the short-chain model of **1d** with DBA groups. Thus, the longest-wavelength absorption bands of **1e–f**, which correspond to the lowest-energy electronic transitions from the HOMO to the LUMO, can be assigned to π–π*-type ICT transitions as in **1d**. The LUMO energy levels of **1e** and **1f** are nearly identical but the HOMO energy level of **1e** slightly exceeds that of **1f**. The difference between the HOMO energy levels can be related to differences in the electron-donating effects of the amino groups attached to the benzene rings, suggesting that the ACE group is a slightly stronger electron-donating amino group than the DPA group. The HOMO–LUMO energy gap is slightly smaller in **1e** than in **1f**, mainly reflecting the differences in HOMO energy levels between the two compounds. The HOMO-to-LUMO electronic transition energies in **1e** and **1f**, namely, the theoretical $\lambda_{max}^{Abs.}$ values, were determined as 449 and 442 nm, respectively, supporting the slight redshift of the experimental $\lambda_{max}^{Abs.}$ value of **1e** from that of **1f**.

As the solvent polarity increased, both compounds showed strong positive fluorosolvatochromism with a large redshift of the fluorescence band, increased bandwidth and Stokes shift, and decreased quantum yield (Φ). The redshift of the fluorescence maximum $\lambda_{max}^{Flu.}$ (~70 nm) was directly visualized as changes in the fluorescence color: the emission of **1e** changed from green to yellow to orange whereas that of **1f** changed from green to yellowish green to yellowish orange. The fluorosolvatochromic behavior of **1e–f** clarifies that the fluorescence of each molecule originates from the highly dipolar ICT excited state,

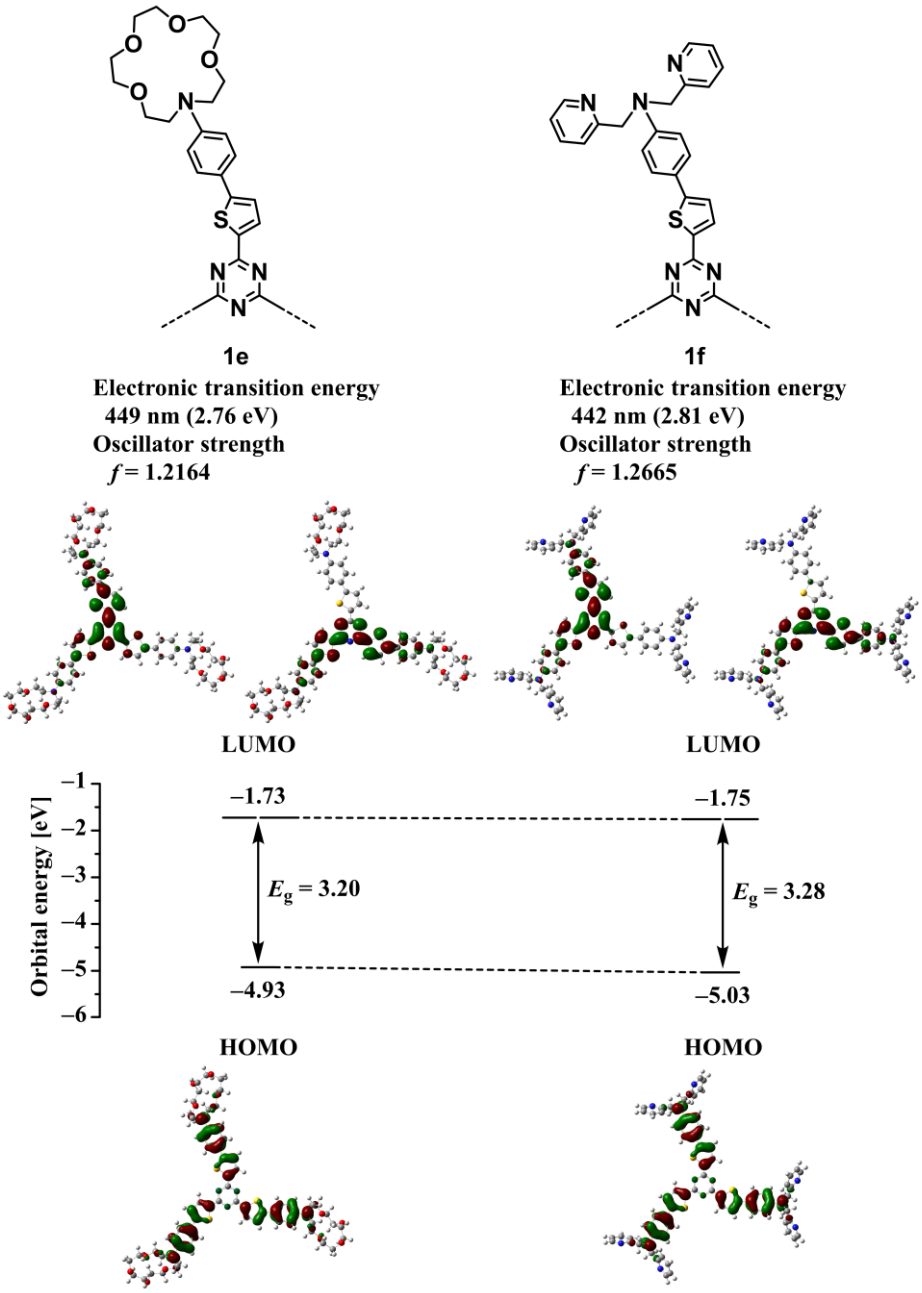

Figure 7. Molecular orbital energy diagrams and isodensity surface plots of **1e–f** optimized at the B3LYP/3-21G(d) level. Also shown are the electronic transition energies and oscillator strengths of the optimized structures, calculated at the time-dependent (TD)-B3LYP/6-31+G(d) level.

which is strongly stabilized by dipole–dipole interactions as the surrounding dipolar solvent molecules reorient. The Lippert–Mataga plots of **1e–f** (Figure 6) were linear with a positive slope, demonstrating that photoexcitation increases the dipole moments of both compounds. From the Lippert–Mataga equation, the dipole moment change ($\Delta\mu$) from the ground to the ICT excited state was calculated as 27.7 D in **1e** and 27.4 D in **1f**. In these calculations, the slopes of the Lippert–Mataga plots of **1e** and **1f** were 6,309 and 6,178 cm^{-1}, respectively, and the Onsager cavity radius of **1e–f** was determined as 10.7 Å, the

approximate molecular radius. Assuming the theoretical dipole moments of the ground states of **1e** and **1f** (μ_g = 2.0 D and 0.0 D, respectively), the dipole moments of the ICT excited states were obtained as μ_e = 29.7 D and 27.4 D, respectively. As observed for **1d**, the μ_e values of both compounds were large and supposedly originated from a photo-induced symmetry-breaking ICT process within the C_3-symmetrical (D–π)$_3$–A structure. The fluorosolvatochromic sensitivity, expressed as the slope of the Lippert–Mataga plot, decreased in the order of **1d** >**1e** ≈**1f**. This trend might arise from the electron-donating strength of the amino group on the benzene ring, which decreased in the order of DBA >ACE ≈DPA owing to the HOMO energy levels of **1d–f**. The slightly weaker electron-donating abilities of ACE and DPA than of DBA probably reflect the inductive electron-withdrawing effects of the two electronegative ether-oxygen atoms and the two electron-deficient pyridinyl groups, which reduce the electron density of the amino-nitrogen atom through the alkylene spacer.

By investigating the effect of solvent polarity on the optical properties of **1d–f**, we demonstrated that **TATTs** incorporating aryl groups with a strong amino-electron-donating substituent exhibited both weak solvatochromism and strong fluorosolvatochromism, which originate from their ICT characteristics. The ICT characteristics depends on the introduced amino-electron-donating group, providing an inherent sensitivity to polarity and observable changes in solution and emission colors. The remarkable fluorosolvatochromism for C_3-symmetrical non-polar **TATTs** arise from the symmetry breaking and large polarity (dipole moment) change in the ICT excited state. By virtue of their solvatochromic and fluorosolvatochromic phenomena, **TATTs** can be exploited as colorimetric and fluorometric probes for detecting environmental polarity.

2-4. Optical sensing responses of TATTs to protons

The ICT process in D–π–A molecules allows the detection of specific ions and molecules.[20] For instance, cations such as protons and metal ions can be optically detected via the amino-donor-type cation receptor in D–π–A molecules, because the coordination of the lone pair on the amino nitrogen atom to the cation diminishes the electron-donating ability of the amino group, thereby suppressing the ICT process in the D–π–A system. Consequently, both the ICT-based absorption and fluorescence bands are dramatically blue-shifted. As an optical spectral shift in the visible-wavelength region results in an optical color change, the chromogenic and fluorogenic D–π–A molecules function as ICT-based colorimetric and fluorometric sensors for the visual detection of cations. Solvatochromic studies has revealed that compounds **1d–f** with strong electron-donating amino terminals possess the strong ICT characteristics induced by the (D–π)$_3$–A skeleton. Based on this fact, in the presence of cations, they elicit an optical response based on the ICT on–off switching mechanism. As the amino terminals are proton-receptor sites,

the chromogenic and fluorogenic compounds **1d–f** will likely function as a colorimetric and fluorometric proton sensors that allow visual detection of protons based on their protonation behavior. Thus, the proton-sensing properties of **1d–f** were investigated by monitoring the UV–vis absorption and fluorescence spectral changes of the compounds after adding trifluoroacetic acid (TFA) as a proton source.[7]

The optical spectral responses of **1d** to protons are illustrated in Figure 8 and their data are summarized in Table 6.

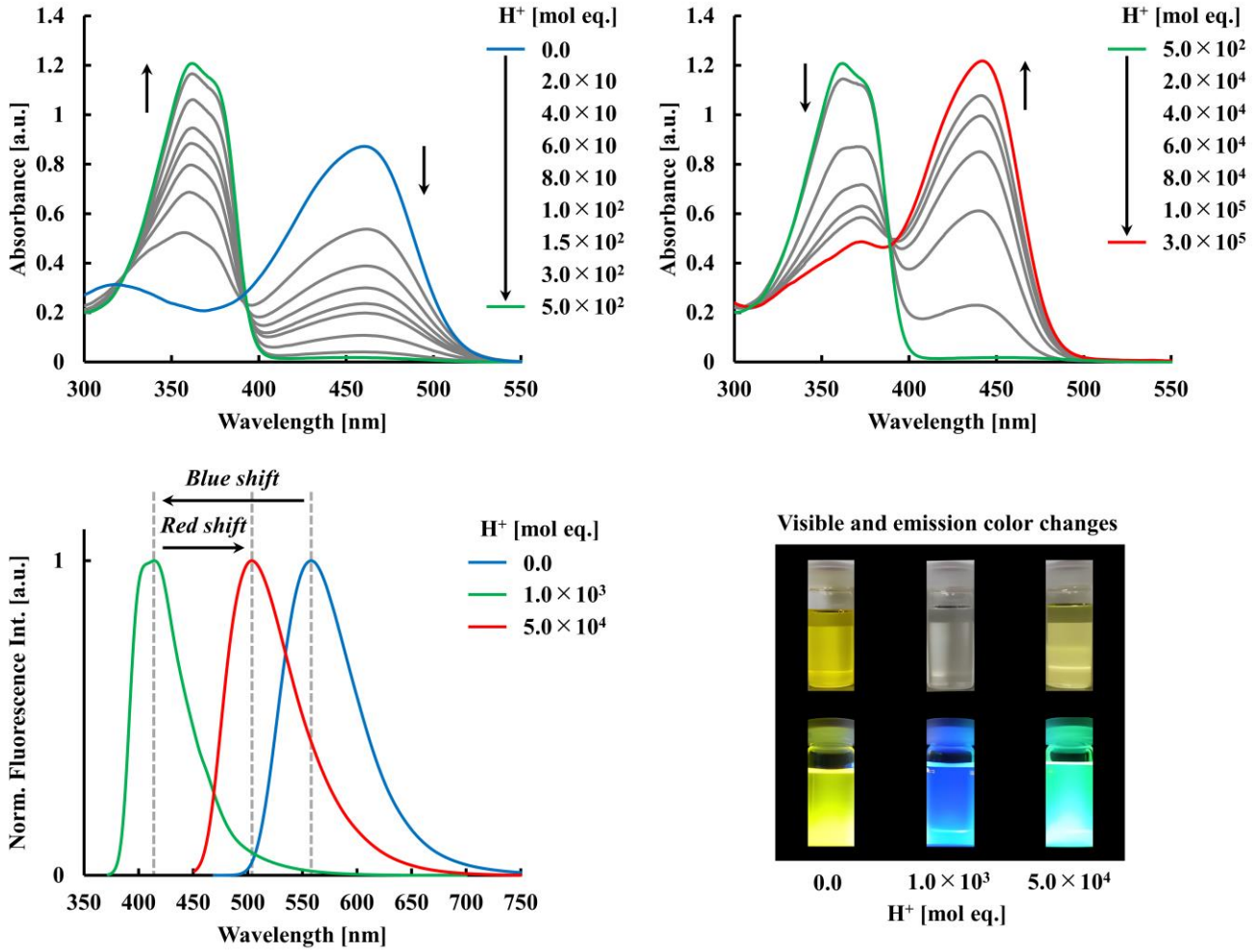

Figure 8. First-step (top left) and second-step changes (top right) in the UV–vis absorption spectrum of **1d** in CH_2Cl_2 solution and the corresponding changes in the normalized fluorescence spectrum (bottom left) upon gradual addition of TFA. Photographs of **1d** in CH_2Cl_2 solution before and after TFA addition under room light and UV light (365 nm) (bottom right).

Table 6. Optical data of **1d** in the presence of protons[a]

Equiv. of proton [mol eq.]	$\lambda_{max}^{Abs.b}$ [nm]	$\lambda_{max}^{Flu.b}$ [nm]	$\Phi^{b,c}$ [–]	Stokes shift [nm (cm^{-1})]
0.0	459	558	0.10	99 (3,865)
1.0×10^3	362	415	0.07	53 (3,528)
5.0×10^4	441	503	0.12	62 (2,795)

[a]The proton source was trifluoroacetic acid (TFA). [b]Measured for a 10 μmol dm^{-3} sample in CH_2Cl_2 solution. Excitation at maximum absorption wavelength ($\lambda_{max}^{Abs.}$). [c]Absolute fluorescence quantum yield determined by a calibrated integrating sphere system.

As TFA was gradually added to CH_2Cl_2 solution, the original absorption band at $\lambda_{max}^{Abs.}$ = 459 nm was progressively attenuated while a new blue-shifted absorption band emerged at $\lambda_{max}^{Abs.}$ = 362 nm. With further TFA addition, the blue-shifted absorption band was progressively attenuated while a new redshifted absorption band appeared at $\lambda_{max}^{Abs.}$ = 441 nm. A similar two-step shift was observed at $\lambda_{max}^{Flu.}$ = 558 nm, which was initially blue-shifted to $\lambda_{max}^{Flu.}$ = 415 nm and then redshifted to $\lambda_{max}^{Flu.}$ = 503 nm. These proton-induced optical spectral shifts manifested as significant color changes in the solutions (from yellow to colorless to pale yellow) and emissions (from yellow to blue to green).

To elucidate the details of the two-step optical response to protons, the ^{13}C NMR signals were monitored while adding TFA-*d* to a solution of **1d** in CD_2Cl_2 (Figure 9). Until the emission color of the solution changed from yellow to blue, the *a* signal corresponding to the carbon atom adjacent to the amino nitrogen atom shifted down-field (from 50.8 to 59.3 ppm). At this time, the *b* signal corresponding to the carbon in the 1,3,5-triazine ring was marginally shifted (from 167.1 to 167.4 ppm). After further addition of TFA-*d* until the emission color of the solution changed from blue to green, the *b* signal shifted up-field (from 167.4 to 162.7 ppm). The first spectral change with no change in the number of signals confirms that the first protonation occurred on the three amino-nitrogen atoms because the C_3-symmetry of **1d** remained intact in the initial protonated state. The second spectral change with no change in the number of signals was interpreted as further protonation on one of the three nitrogen atoms, not on all three nitrogen atoms in the 1,3,5-triazine ring. A trication state generated by protonation of all three 1,3,5-triazinyl nitrogen atoms was expected to be destabilized by Coulombic repulsion among the three positive charges. The pseudo-C_3-symmetry of the further protonated state can be explained by fast protonation–deprotonation equilibrium among the 1,3,5-triazinyl nitrogen atoms.[21] After adding triethylamine (TEA) as a basic source to the green-emissive solution containing **1d** protonated with TFA-*d*, the original spectrum was successfully recovered because **1d** was regenerated by stepwise

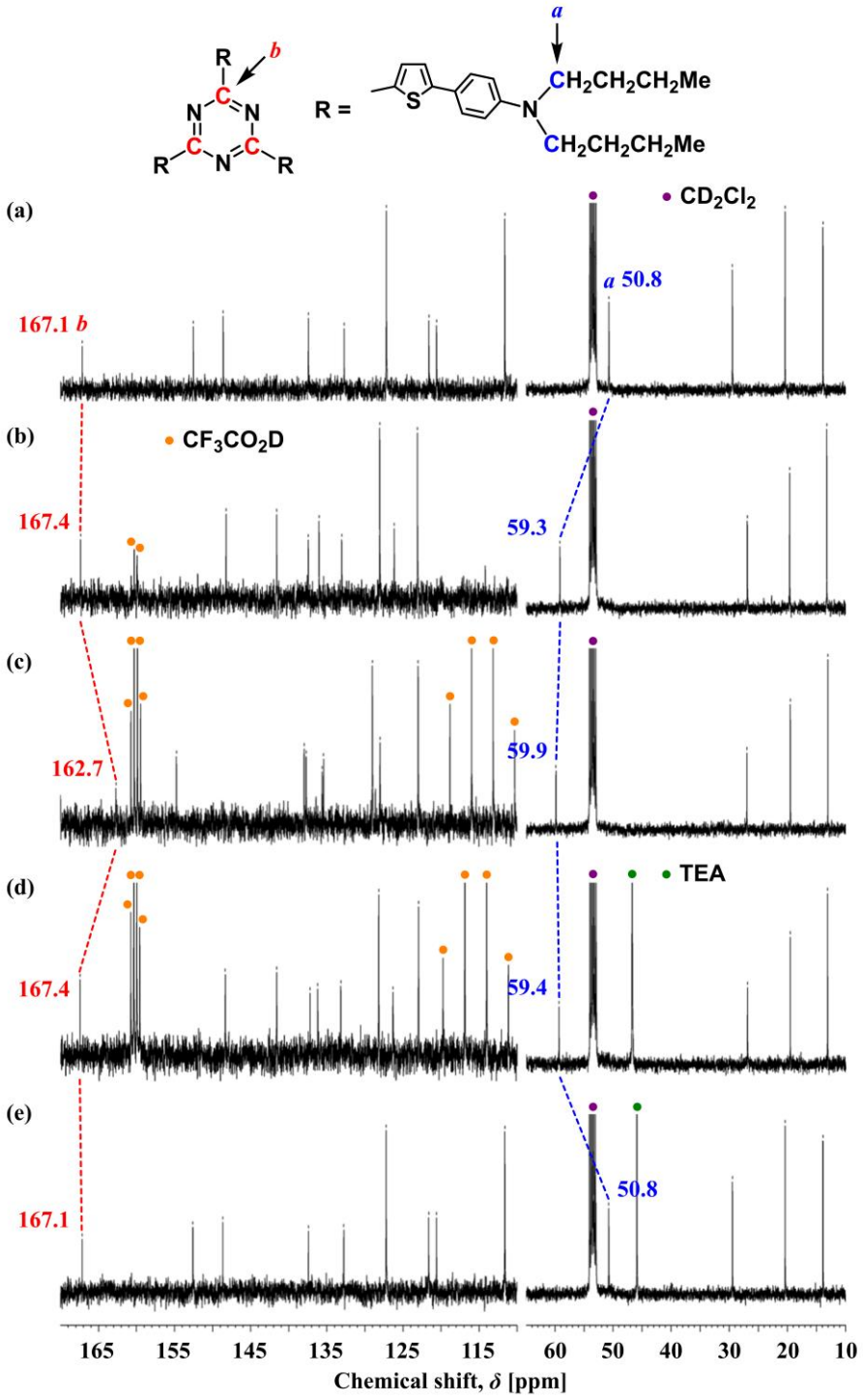

Figure 9. Selected carbon atoms in **1d** for determining the protonation site (top). ^{13}C NMR signals of **1d** and their shifts caused by protonation and deprotonation (bottom): (a) 5 mg of **1d** in 0.75 mL CD_2Cl_2, (b) addition of 3 μL of trifluoroacetic acid-*d* (CF_3CO_2D), (c) further addition of 27 μL of CF_3CO_2D, (d) addition of 20 μL of triethylamine (TEA), (e) further addition of 40 μL of TEA. The ^{13}C NMR spectrum in (e) was measured after washing with D_2O to remove the deposited ammonium salt between TFA-*d* and TEA.

deprotonation with TEA. This recovery was accompanied by a change to the original yellow-emissive solution. This result demonstrates that protonation–deprotonation reactions of **1d** can be reversed without any decomposition reactions.

To better understand the proton-sensing mechanism, MO calculations were performed on **1d′ + 3H**$^+$ and **1d′ + 4H**$^+$, the short-chain models of the protonated states **1d + 3H**$^+$ with three protonated amino-nitrogen atoms and **1d + 4H**$^+$ with one further protonated 1,3,5-triazinyl nitrogen atom, respectively (Figure 10).[11] Both the HOMO (doubly degenerated) and LUMO (doubly degenerated) in the C_3-symmetrical **1d′ + 3H**$^+$ model are widely delocalized and spread over the whole star-shaped π-conjugated backbone, clarifying that the electronic HOMO-to-LUMO transition corresponds to the π–π* transition with no ICT contribution. The HOMO–LUMO energy gap is higher in **1d′ + 3H**$^+$ than in **1d′**, indicating that the HOMO is more strongly stabilized than the LUMO by the electron-accepting effect of the ammonium-nitrogen atom. Meanwhile, the HOMO of C_1-symmetrical **1d′ + 4H**$^+$ delocalizes around the protonated 1,3,5-triazine core, the three thiophene spacers, and one of the three aryl groups, whereas the LUMO is mostly concentrated in the protonated triazine core and the three thiophene spacers, overlapping some regions of the HOMO. Thus, the electronic HOMO-to-LUMO transition is dominated by π–π* transitions within the protonated 1,3,5-triazine and its three adjacent thiophene moieties. When the 1,3,5-triazinyl nitrogen atom in **1d′ + 3H**$^+$ is additionally protonated to **1d′ + 4H**$^+$, both the HOMO and LUMO energy levels are further stabilized by the enhanced electron-accepting effect of the 1,3,5-triazinium nitrogen atom, but the stronger stabilization of the LUMO than the HOMO decreases the HOMO–LUMO energy gap. The electronic HOMO-to-LUMO transition energies of the initially protonated **1d′ + 3H**$^+$ and additionally protonated **1d′ + 4H**$^+$ were estimated as 369 and 446 nm, respectively. These transition energies correspond to the theoretical $\lambda_{max}^{Abs.}$ values, which are close to the experimental $\lambda_{max}^{Abs.}$ values in each state. This fact proves that the proton-induced two-step absorption spectral change of **1d** manifests from stepwise protonation of the three amino-nitrogen atoms and one 1,3,5-triazinyl nitrogen atom.

Figure 11 summarizes the two-step protonation behavior of **1d** and its associated two-step optical response. The blue-shift of the absorption and fluorescence bands in the first protonation step is induced by protonation of the amino-nitrogen atoms. The HOMO–LUMO energy gap increases because the electron-donating ability of the amino terminals diminishes, causing a blue-shift of the absorption band assigned to the higher-energy π–π* transition with a suppressed ICT. The blue-shifted fluorescence band originates from the emission of the π–π* excited state, which is much more destabilized than the ICT excited state before the first protonation. The redshift of the absorption and fluorescence bands in the

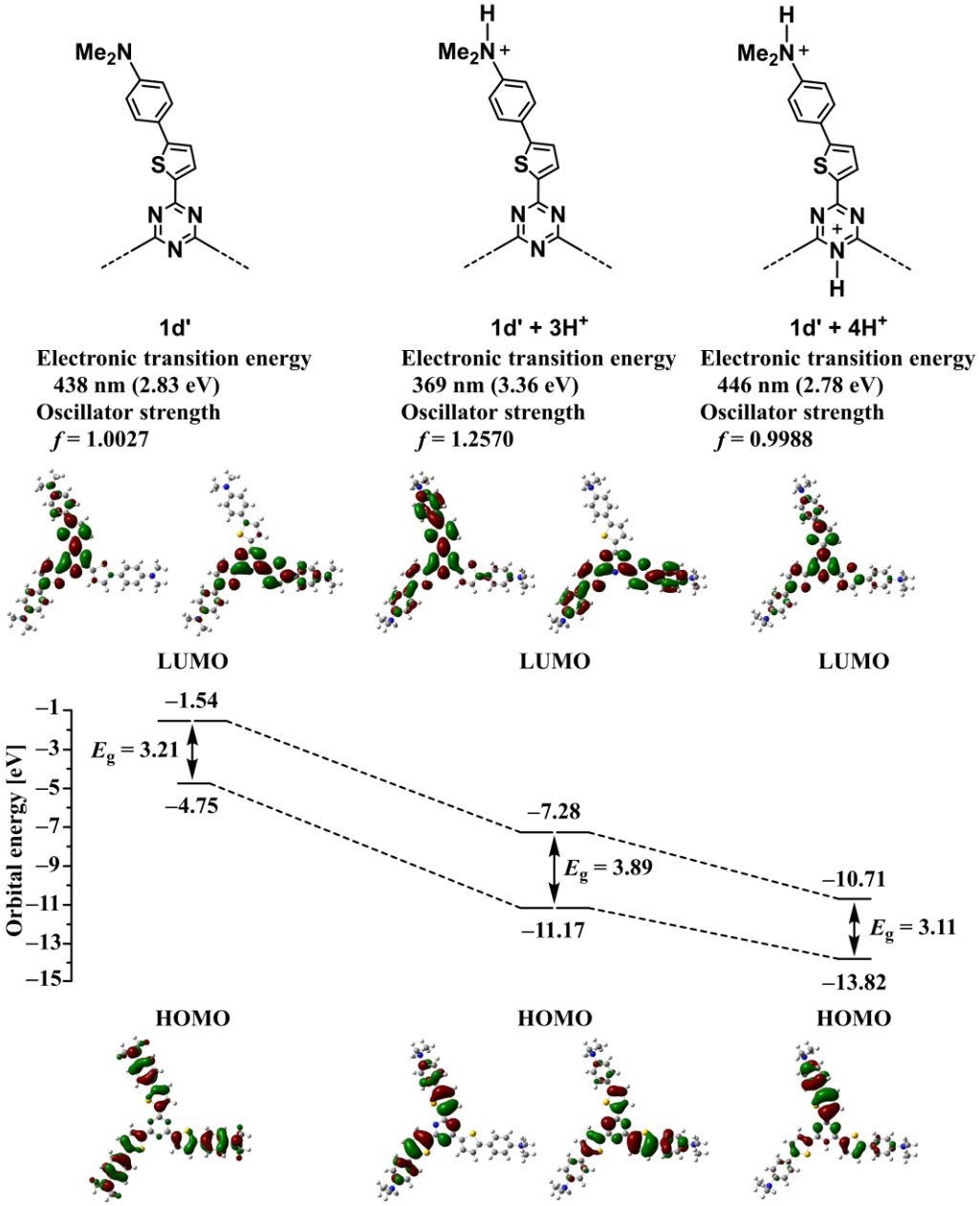

Figure 10. Molecular orbital energy diagrams and isodensity surface plots of **1d′** and its two protonated states (**1d′ + 3H**$^+$ and **1d′ + 4H**$^+$) optimized at the B3LYP/3-21G(d) level. Also shown are the electronic transition energies and oscillator strengths of each optimized structure, calculated at the time-dependent (TD)-B3LYP/6-31G(d,p) level.

second step is induced by further protonation of the 1,3,5-triazinyl nitrogen atom. The HOMO–LUMO energy gap decreases because the electron-accepting ability of the 1,3,5-triazine core increases, causing a redshift of the absorption band assigned to the lower-energy π–π* transition. The redshifted fluorescence band originates from the emission of the π–π* excited state, which is more strongly stabilized than before the second protonation.

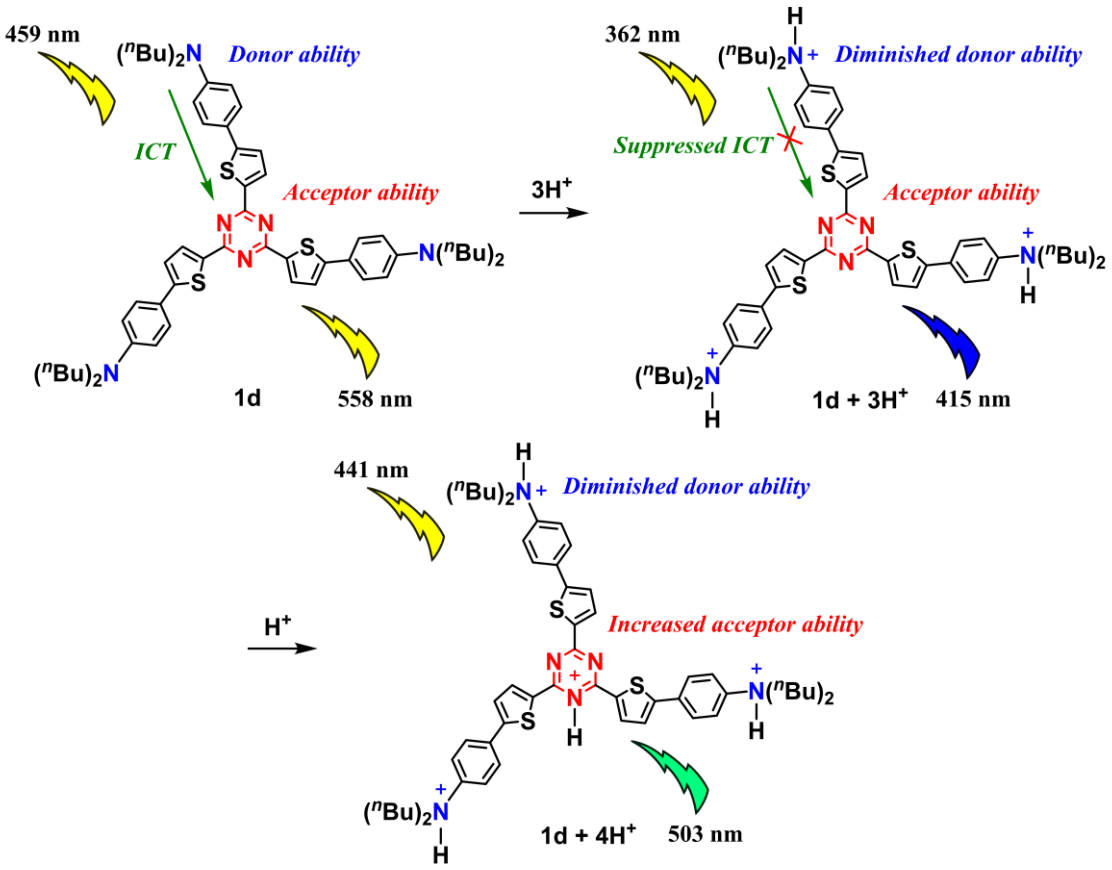

Figure 11. Possible proton-sensing mechanism of **1d**

We then investigated the proton-sensing properties of **1e** and **1f** with the ACE and DPA receptors, respectively. The proton sensitivities of ACE and DPA differ from that of the DBA receptor. The UV–vis absorption and fluorescence spectra of the receptors in proton-containing CH_2Cl_2 solution are shown in Figures 12 and 13 and the data are presented in Table 7.

As TFA was gradually added to the CH_2Cl_2 solution of **1e**, the original absorption and fluorescence bands were blue-shifted from $\lambda_{max}^{Abs.}$ = 450 to 361 nm and from $\lambda_{max}^{Flu.}$ = 553 to 416 nm, respectively. The blue-shifts of the absorption and fluorescence bands were followed by redshifts to $\lambda_{max}^{Abs.}$ = 438 nm and $\lambda_{max}^{Flu.}$ = 496 nm, respectively. The solution color changed from yellow to colorless to pale yellow and the fluorescence color changed from yellow to blue to green. These proton-induced optical spectral changes almost coincided with those of **1d** having DBA receptors. Consequently, the two-step optical response of **1e** to protons is reasonably explained by the two-step protonation behavior of **1d**, namely, initial protonation of the three amino-nitrogen atoms in ACE followed by protonation of one 1,3,5-triazinyl nitrogen atom.

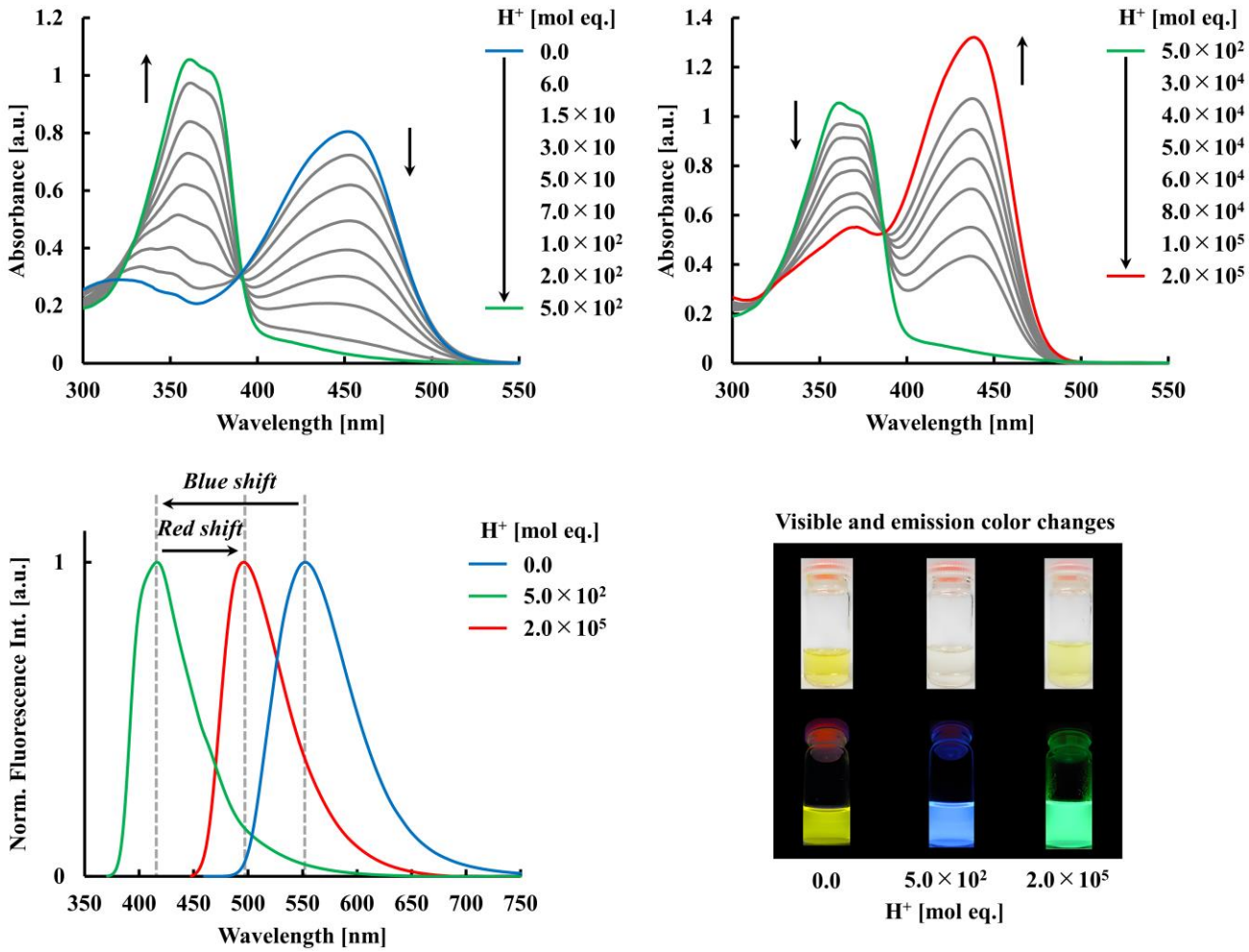

Figure 12. First-step (top left) and second-step changes (top right) in the UV–vis absorption spectrum of **1e** in CH_2Cl_2 solution and the corresponding changes in the normalized fluorescence spectrum (bottom left) upon gradual TFA addition. Photographs of **1e** in CH_2Cl_2 solution before and after TFA addition, taken under room light and UV light (365 nm) (bottom right).

Compound **1f** also exhibited a two-step optical response to protons governed by two-step protonation behavior accompanied by stepwise variations in the solution and emission colors. The solution color changed from yellow to pale-yellow to orange, whereas the emission color changed from yellowish-green to green to red. In the first step, the original absorption and fluorescence bands were blue-shifted from $\lambda_{max}^{Abs.}$ = 435 to 408 nm and from $\lambda_{max}^{Flu.}$ = 547 to 515 nm, respectively. In contrast to **1d–e**, **1f** exhibited an extremely small blue-shift ($\Delta\lambda_{max}^{Abs.}$ = 27 nm; $\Delta\lambda_{max}^{Flu.}$ = 32 nm) resulting from the initial protonation sites (two pyridinyl nitrogen atoms rather than the amino-nitrogen atom on each DPA group).[22] As the enhanced electron-accepting ability of the protonated pyridinyl group slightly decreases the electron-donating ability of the amino group through the methylene spacer, the HOMO is slightly stabilized and the HOMO–LUMO energy gap slightly increases; accordingly, the blue-shift of the

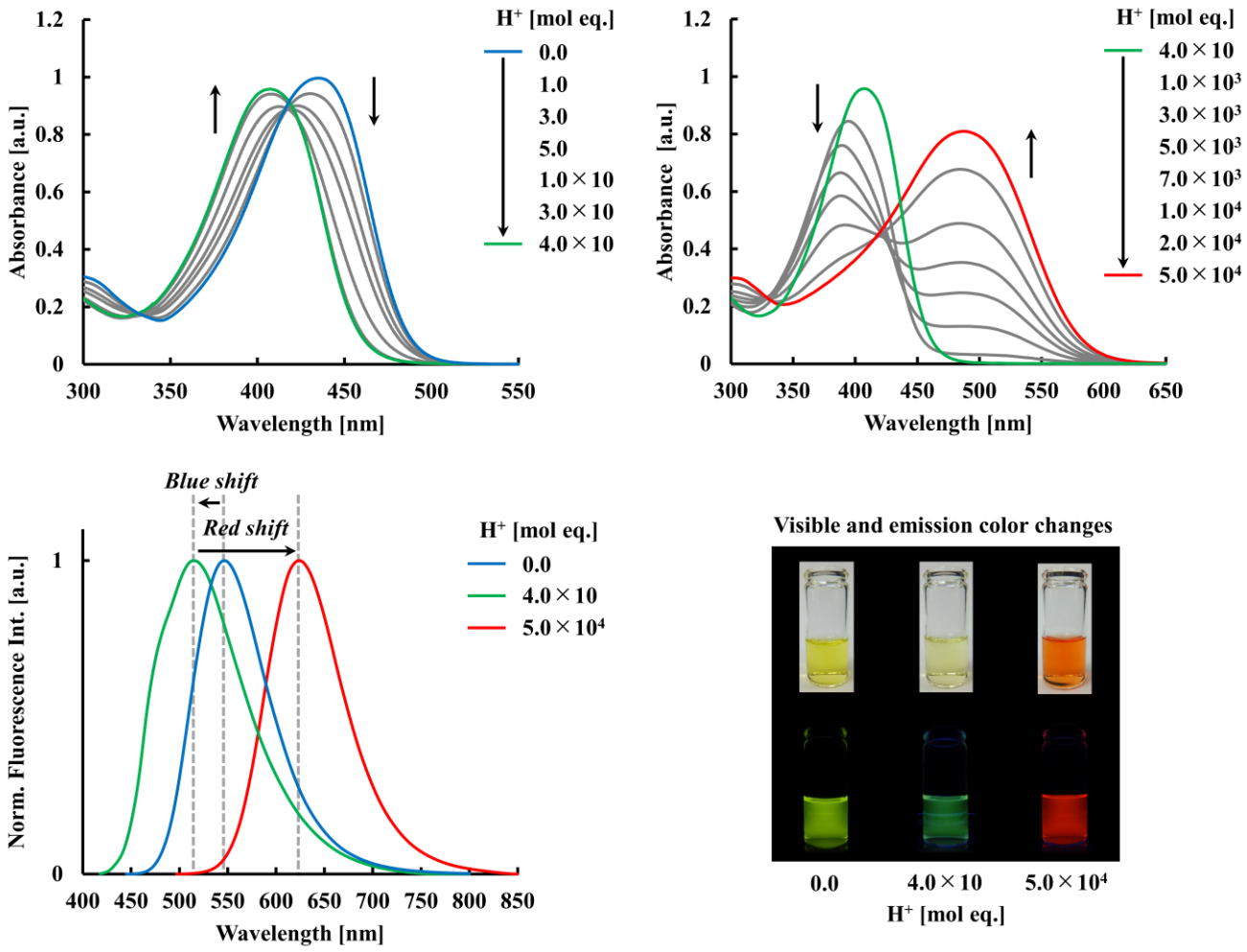

Figure 13. First-step (top left) and second-step changes (top right) in the UV–vis absorption spectrum of **1f** in CH_2Cl_2 solution and the corresponding changes in the normalized fluorescence spectrum (bottom left) upon gradual TFA addition. Photographs of **1f** in CH_2Cl_2 solution before and after TFA addition, taken under room light and UV light (365 nm) (bottom right).

ICT-based absorption band is small. The slight decrease of the electron-donating effect of the amino group also slightly decreases the ICT efficiency in the excited state, causing a small blue-shift in the ICT-based fluorescence band. In the second protonation step, the blue-shifted absorption and fluorescence bands were redshifted to $\lambda_{max}^{Abs.}$ = 487 nm and $\lambda_{max}^{Flu.}$ = 624 nm, respectively. The large redshift ($\Delta\lambda_{max}^{Abs.}$ = 79 nm; $\Delta\lambda_{max}^{Flu.}$ = 109 nm) results from further protonation of one 1,3,5-triazinyl nitrogen atom. The enhanced electron-accepting ability of the protonated 1,3,5-triazine core largely decreases the HOMO–LUMO energy gap by largely stabilizing the LUMO. Furthermore, it largely increases the ICT efficiency in the excited state because the unprotonated amino groups retain their electron-donating ability. Therefore, the ICT-based absorption and fluorescence bands are largely redshifted.

Table 7. Optical data of **1e–f** in the presence of protons[a]

TATT	Equiv. of proton [mol eq.]	$\lambda_{max}^{Abs.b}$ [nm]	$\lambda_{max}^{Flu.b}$ [nm]	$\Phi^{b,c}$ [–]	Stokes shift [nm (cm^{-1})]
1e	0.0	450	553	0.08	103 (4,139)
	5.0×10^2	361	416	0.10	55 (3,663)
	2.0×10^5	438	496	0.27	58 (2,670)
1f	0.0	435	547	0.05	112 (4,707)
	4.0×10	408	515	< 0.01	107 (5,093)
	5.0×10^4	487	624	0.01	137 (4,508)

[a]The proton source was TFA. [b]Measured for a 10 μmol dm^{-3} sample in CH_2Cl_2 solution. Excitation at maximum absorption wavelength ($\lambda_{max}^{Abs.}$). [c]Absolute fluorescence quantum yield determined by a calibrated integrating sphere system.

Figure 14 summarizes the two-step protonation behavior of **1e** and **1f** and their associated two-step optical responses. Both compounds displayed proton-induced optical spectral blue-shifts followed by redshifts, but the degree of these shifts largely depended on the intrinsic two-step protonation behavior of the compounds. The difference in the overall spectral shifts is explained by differences in the initial protonation sites, triggering different ICT natures during the stepwise protonation reaction and eliciting different two-step color changes in the absorption and emission visualizations.

In summary, compounds **1d–e** with the DBA and ACE receptors exhibited colorimetric and fluorometric responses to protons. The two-step protonation behavior manifested as stepwise changes in the solution and emission colors. This two-step proton response arises not only from the amino-nitrogen atoms but also from the proton-accepting imino-nitrogen atom in the 1,3,5-triazine ring. Compound **1f**, in which the pyridinyl nitrogen atoms possess higher proton-sensitivity (basicity) than the amino nitrogen atom in the DPA receptor, exhibited a different proton-sensing mechanism and different two-step colorimetric and fluorometric responses to protons. Overall, **TATTs** with their amino terminals and 1,3,5-triazine core are potentially usable as proton-responsive optical sensors displaying stepwise color changes together with two-step optical spectral shifts.

2-5. Optical sensing responses of TATTs to metal ions

The on–off switching of the ICT process, determined by the binding functionality of the amino-donor-type receptor incorporated into the D–π–A molecule, enables the detection of cations. ACE[23] with binding affinities for Ca^{2+} and Mg^{2+} and DPA[24] with a binding affinity for Zn^{2+} are suitable

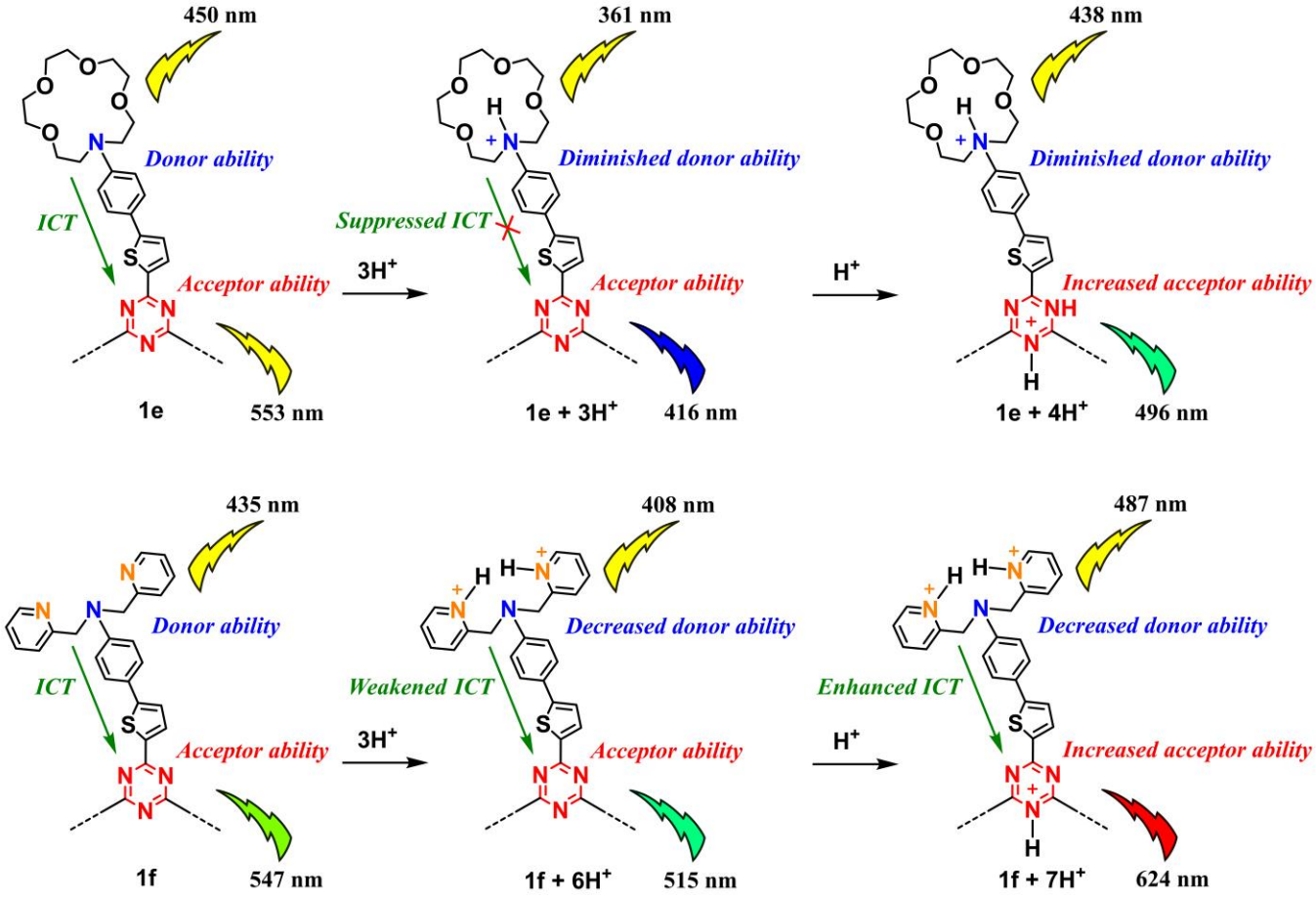

Figure 14. Possible proton-sensing mechanisms of **1e–f**

amino-donor-type receptors for building the D–π–A molecule, as they optically respond to specific cations. As already confirmed, **TATTs 1e–f** with their ACE and DPA receptors detect protons at both the receptor (electron-donor) and core (electron-acceptor) sites, eliciting an ICT-based optical response involving two-step optical spectral shifts accompanied by stepwise visual color changes. Therefore, compounds **1e–f** are expected to exhibit an ICT-based optical response toward specific metal ions depending on their binding affinity. Additionally, if a metal ion binds to the 1,3,5-triazine core after first binding to the ACE or DPA terminals, single metal ions will elicit a stepwise optical response similar to that of protons. From this standpoint, we investigated the metal-ion-sensing properties of **1e–f** in a mixed solution of CH_2Cl_2 and MeCN (1: 1 v/v). The UV–vis absorption and fluorescence spectral changes after adding Mg^{2+} or Ca^{2+} perchlorate salt to **1e** and a Zn^{2+} perchlorate salt to **1f** are presented in Figures 15, 16 and 17. The data are given in Table 8.[7b]

The gradual addition of Mg^{2+} induced a two-step change in the UV–vis absorption spectrum of compound **1e**. In the first step, the original absorption band at $\lambda_{max}^{Abs.}$ = 451 nm was attenuated while a new

absorption band emerging at $\lambda_{max}^{Abs.}$ = 362 nm was amplified. In the second step, the blue-shifted absorption band was attenuated while a new absorption band at $\lambda_{max}^{Abs.}$ = 438 nm was amplified. A corresponding two-step change appeared in the fluorescence spectrum: a spectral blue-shift from $\lambda_{max}^{Flu.}$ = 577 to 425 nm followed by a spectral redshift from $\lambda_{max}^{Flu.}$ = 425 to 529 nm. Visually, the yellow solution turned colorless and then pale-yellow, whereas the yellow emission turned blue and then green. As the observed two-step optical responses to Mg^{2+} and H^+ are very similar, the Mg^{2+}-sensing mechanism can be understood as follows. Upon initial complexation of the three ACE receptors with Mg^{2+}, the ACE group on the benzene ring loses its electron-donating ability because the lone pair on the amino nitrogen atom coordinates to Mg^{2+}, leading to complete suppression of the ICT process. This process gives rise to the

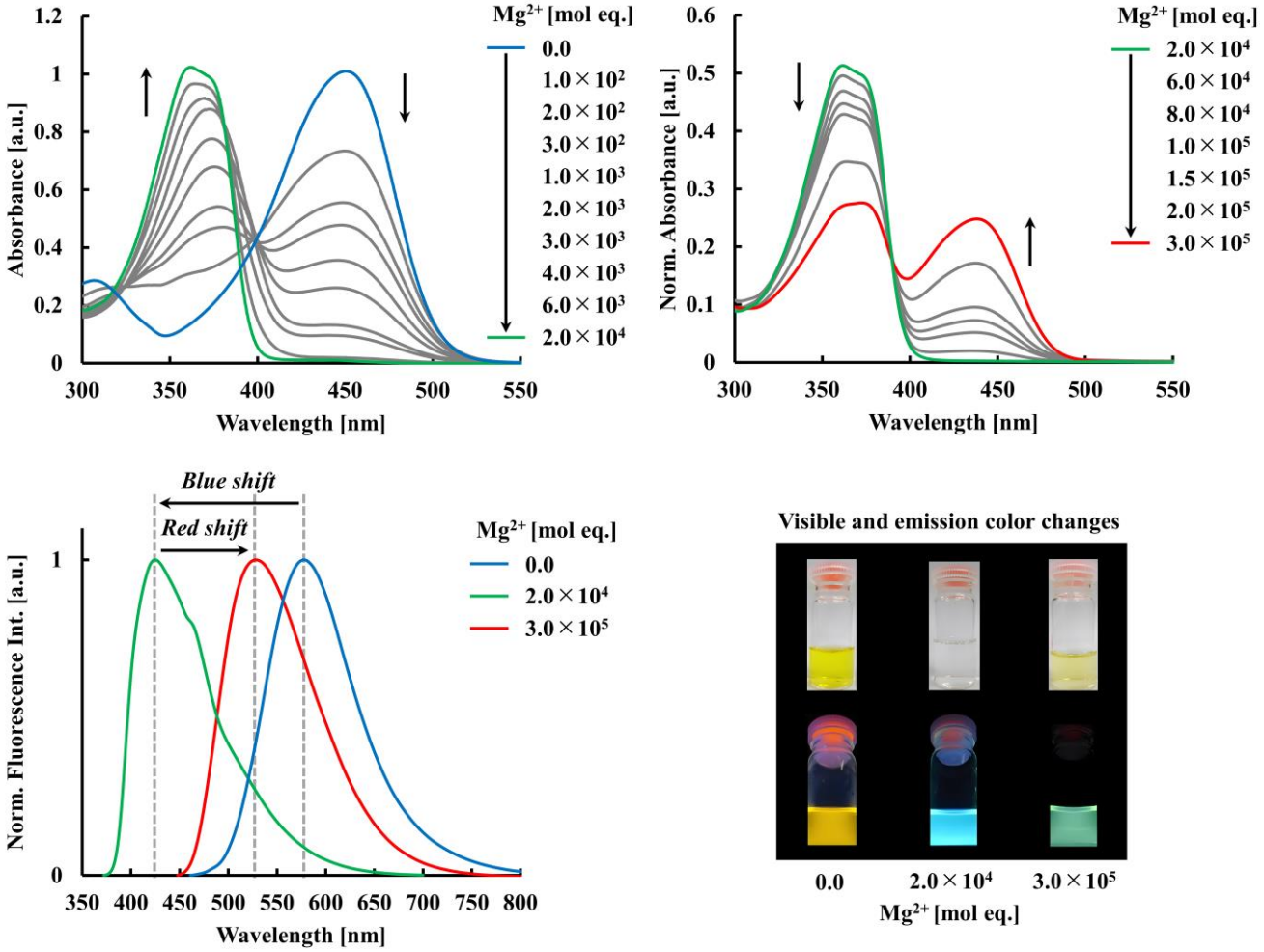

Figure 15. First-step (top left) and second-step changes (top right) in the UV–vis absorption spectrum of **1e** in CH_2Cl_2–MeCN solution (1: 1 v/v) and the corresponding changes in the normalized fluorescence spectrum (bottom left) upon gradual addition of $Mg(ClO_4)_2$. Photographs of **1e** in the CH_2Cl_2–MeCN solution before and after $Mg(ClO_4)_2$ addition, taken under room light and UV light (365 nm) (bottom right).

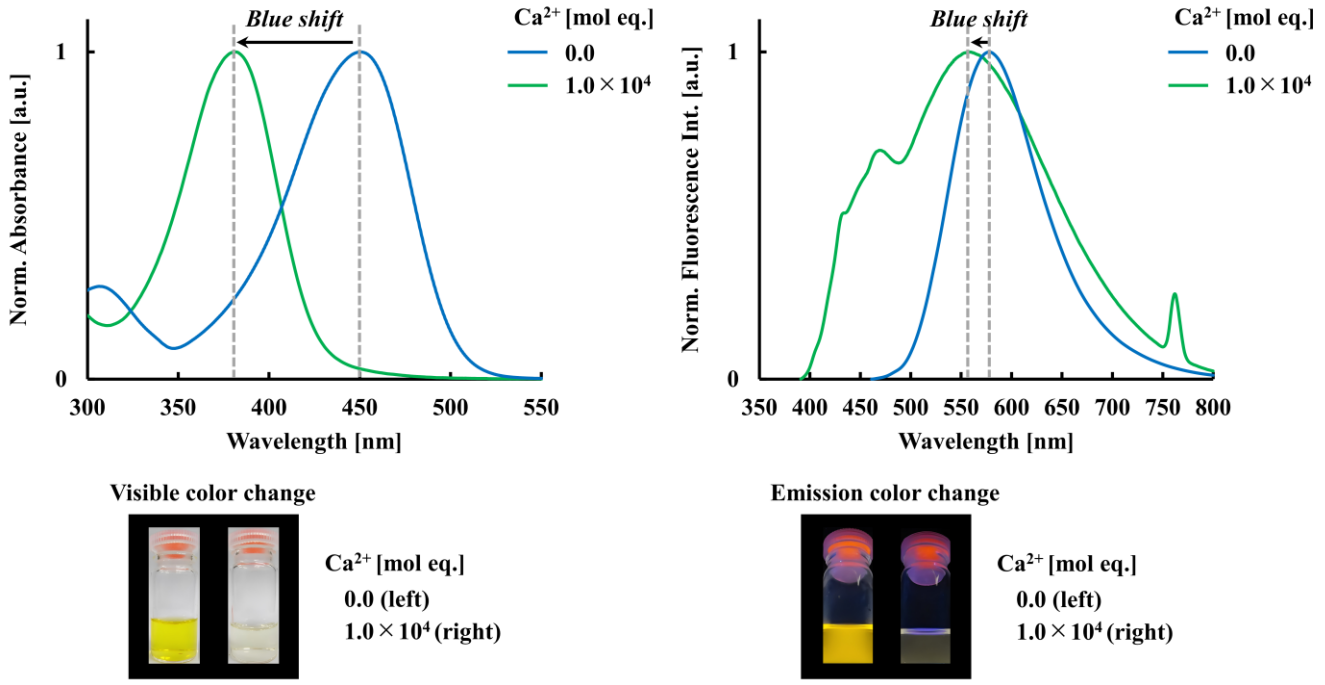

Figure 16. Changes in the normalized UV–vis absorption (top left) and normalized fluorescence (top right) spectra of **1e** in CH_2Cl_2–MeCN solution (1: 1 v/v) upon $Ca(ClO_4)_2$ addition. Photographs of **1e** in CH_2Cl_2–MeCN solution (1: 1 v/v) before and after $Ca(ClO_4)_2$ addition, taken under room light (bottom left) and UV light (365 nm) (bottom right).

first shifts (blue shifts) in the absorption and fluorescence spectra. The 1,3,5-triazine core then complexes with Mg^{2+} to form a thermodynamically favorable σ complex,[25] inducing the second shifts (redshifts) in the absorption and fluorescence spectra. The coordination interaction between the lone pair on the 1,3,5-triazinyl nitrogen atom and Mg^{2+} enhances the electron-accepting ability of the 1,3,5-triazine core. In contrast, Ca^{2+} addition induces a large blue shift of the original absorption band from $\lambda_{max}^{Abs.}$ = 451 to 381 nm (70 nm), indicating that the three ACE receptors are completely complexed with Ca^{2+}. The formation of this coordination bond decreases the electron-donating ability of the amino-nitrogen atom within the ACE receptor. The fluorescence band of the complexed **1e** was blue-shifted by 19 nm from that of the original **1e**. This shift, from $\lambda_{max}^{Flu.}$ = 577 nm to 558 nm, was much smaller than the blue-shift of $\lambda_{max}^{Abs.}$. Additionally, the blue-shifted fluorescence intensity was very low and the fluorescence quantum yield (Φ) could not be determined; accordingly, the complex of **1e** with three Ca^{2+} ions was essentially non-emissive. These optical features suggest that the ICT process and the succeeding cation-ejection process combine into a relaxation process that converts the FC excited state to a relaxed ICT (RICT) excited state with very weak fluorescence.[26] More specifically, during relaxation from the FC excited state, the ICT proceeds through three steps: i) delocalization of the electron-donating lone pair on the amino-nitrogen atom to the electron-accepting 1,3,5-triazine core across the π-conjugated linker, ii)

cleavage of the coordination bond between the amino-nitrogen atom and Ca^{2+}, and iii) formation of the push–pull π-conjugated structure containing the positively charged iminium-nitrogen atom. The cation-ejection process is driven by electrostatic repulsion between the two positively charged cations (iminium-nitrogen and Ca^{2+}). When the Ca^{2+} ion is released from the azacrown cavity, the FC excited state finally reaches the RICT excited state. The blue-shift of the fluorescence band of **1e** after complexing with three Mg^{2+} cations was large and intense, demonstrating stronger coordination of the amino-nitrogen lone pair to the Mg^{2+} center than to the Ca^{2+} center. The ICT relaxation process is then completely blocked, triggering the photoejection of cations. As Mg^{2+} has a higher ionic potential than Ca^{2+}, the difference in coordination strengths likely originates from the stronger electrostatic attraction of Mg^{2+} than of Ca^{2+}.[27]

During gradual addition of Zn^{2+} to **1f** solution, the UV–vis absorption and fluorescence spectra both displayed a one-step change. The original absorption band at $\lambda_{max}^{Abs.}$ = 437 nm in the UV–vis absorption spectrum was attenuated while a new absorption band at $\lambda_{max}^{Abs.}$ = 374 nm emerged and was amplified. In the fluorescence spectrum, the original fluorescence band at $\lambda_{max}^{Flu.}$ = 569 nm with an extremely low quantum yield (Φ = < 0.01) disappeared while a new fluorescence band with an increased quantum yield

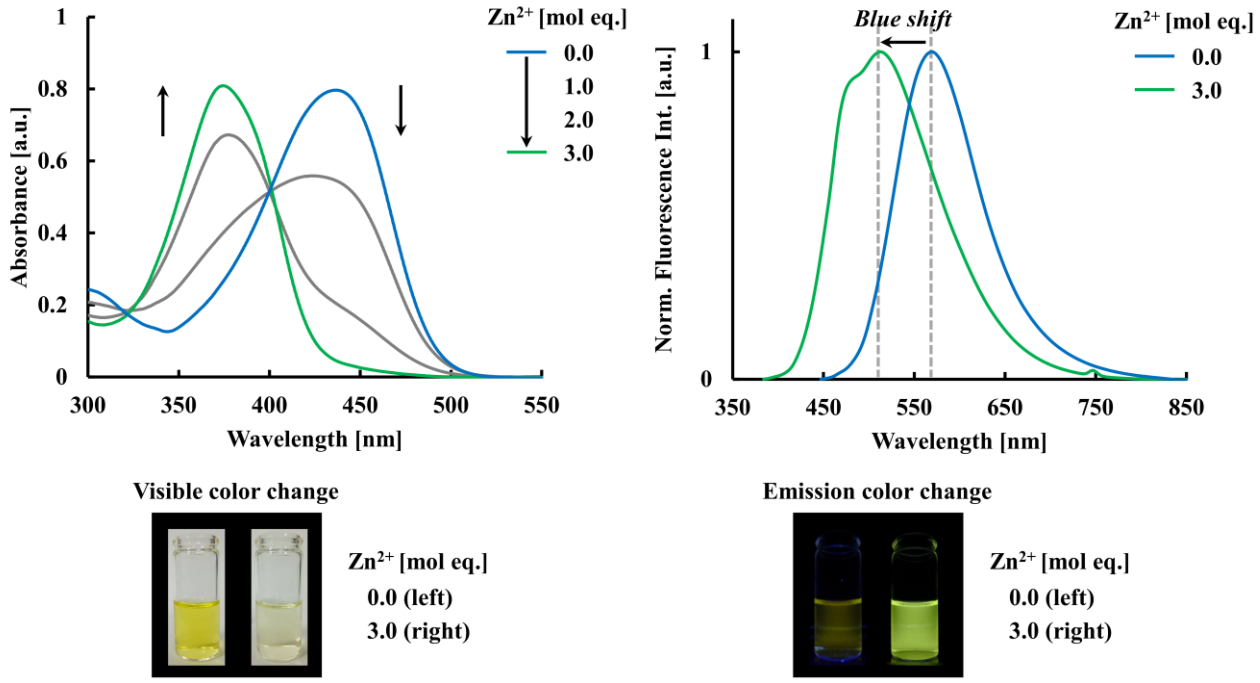

Figure 17. Changes in the UV–vis absorption spectrum of **1f** in CH_2Cl_2–MeCN solution (1: 1 v/v) (top left) and the corresponding changes in the normalized fluorescence spectrum (top right) during $Zn(ClO_4)_2$ addition. Photographs of **1f** in the CH_2Cl_2–MeCN solution before and after $Zn(ClO_4)_2$ addition, taken under room light (bottom left) and UV light (365 nm) (bottom right).

Table 8. Optical data of **1e–f** in the presence of metal ions[a]

TATT	Equiv. of metal ion [mol eq.]		$\lambda_{max}^{Abs.}$[b] [nm]	$\lambda_{max}^{Flu.}$[b] [nm]	Φ[b,c] [–]	Stokes shift [nm (cm^{-1})]
1e		0.0	451	577	< 0.01	126 (4,842)
	Mg^{2+}	2.0×10^4	362	425	0.06	63 (4,095)
		3.0×10^5	438[d]	529[d]	0.07[d]	91 (3,927)
	Ca^{2+}	1.0×10^4	381	558	–[e]	177 (8,326)
1f		0.0	437	569	< 0.01	132 (5,308)
	Zn^{2+}	3.0	374	513	0.02	139 (7,245)
		1.0×10^3	382	507	0.02	125 (6,454)

[a]The metal-ion source was $Mg(ClO_4)_2$, $Ca(ClO_4)_2$, or $Zn(ClO_4)_2$. [b]Measured for a 10 μmol dm^{-3} sample in CH_2Cl_2–MeCN solution (1: 1 v/v). Excitation at maximum absorption wavelength ($\lambda_{max}^{Abs.}$). [c]Absolute fluorescence quantum yield determined by a calibrated integrating sphere system. [d]Measured for a 4.0 μmol dm^{-3} sample in CH_2Cl_2–MeCN solution (1: 1 v/v). [e]Not determined due to very weak fluorescence.

(Φ = 0.02) appeared at $\lambda_{max}^{Flu.}$ = 513 nm. As the blue-shifted absorption and fluorescence bands moved by less than 10 nm even after adding 1.0×10^3 mol eq. of Zn^{2+}, the optical spectral response was terminated at 3 mol eq. of Zn^{2+}. In the presence of Zn^{2+}, the yellow solution became colorless and the dim yellowish-orange emission became a brighter yellowish-green. The Zn^{2+}-induced blue-shifts in the optical spectra are easily interpreted as loss of the electron-donating ability of the DPA group on the benzene ring after complexation of the three DPA receptors with Zn^{2+}, and consequent ICT suppression.

To clarify that the 1,3,5-triazine core can recognize metal ions, we examined the metal-ion binding reactivity of **1a**, which has no amino-donor-type receptor on its benzene rings. The changes in the UV–vis absorption and fluorescence spectra while adding a Ca^{2+}, Mg^{2+}, or Zn^{2+} perchlorate salt to a mixed solution (CH_2Cl_2: MeCN = 1: 1 v/v) of **1a** are displayed in Figure 18 and Table 9. The long-wavelength absorption band assigned to the π–π* transition was redshifted (from $\lambda_{max}^{Abs.}$ = 369 to 450 nm) only after adding Mg^{2+} ions. The corresponding fluorescence band emitted from the π–π* excited state was redshifted from $\lambda_{max}^{Flu.}$ = 436 to 552 nm. Reflecting these optical spectral shifts, the originally colorless solution became pale-yellow and the emission color turned from blue to yellowish-green. These results confirm a coordination interaction between the lone pair on the 1,3,5-triazinyl nitrogen atom and Mg^{2+}, demonstrating that the 1,3,5-triazine core within the star-shaped $(D–\pi)_3$–A molecule functions as a special binding receptor of Mg^{2+}.

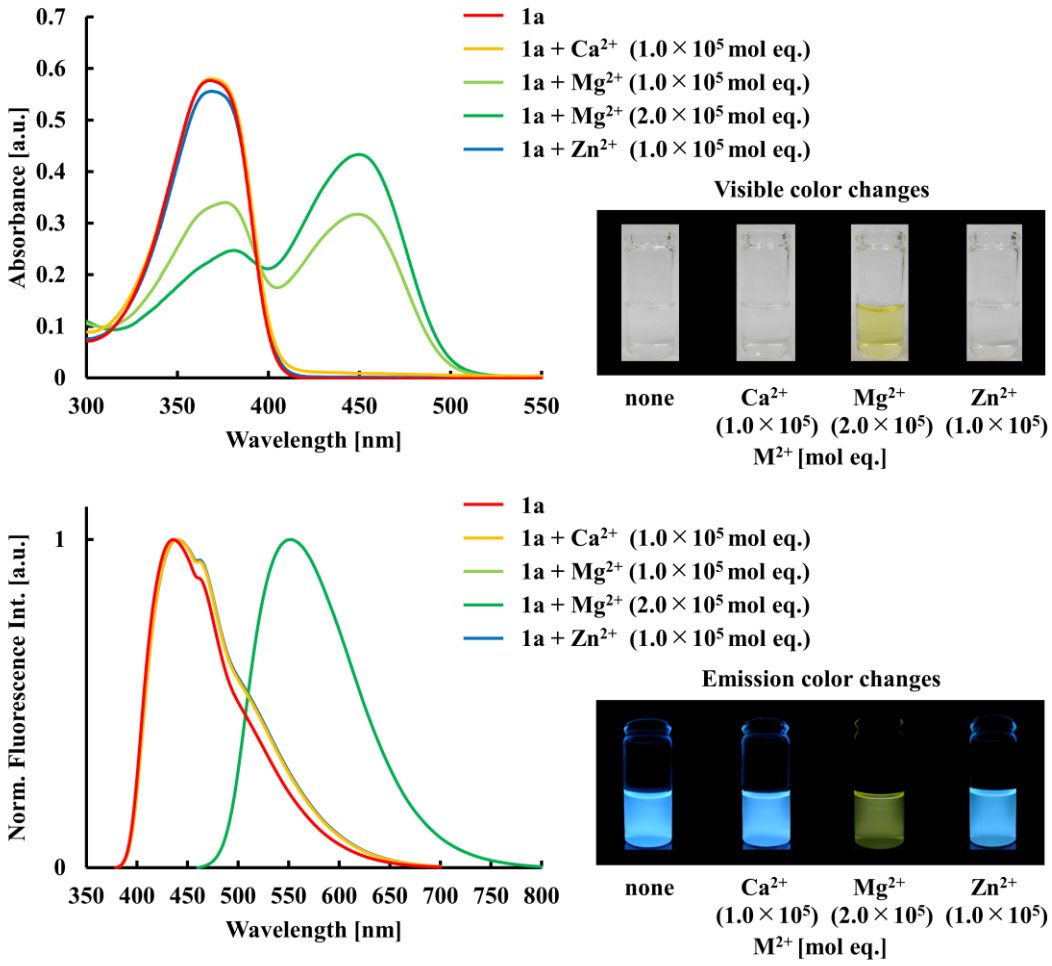

Figure 18. UV–vis absorption (top) and normalized fluorescence (bottom) spectra of **1a** in CH_2Cl_2–MeCN solution (1: 1 v/v) exposed to excess amounts of different metal ions (Ca^{2+}, Mg^{2+}, and Zn^{2+} as perchlorate salts). Inset: photographs of **1a** in the CH_2Cl_2–MeCN solutions containing excess Ca^{2+}, Mg^{2+}, and Zn^{2+} ions, taken under room light and UV light (365 nm).

Table 9. Optical data of **1a** in the presence of metal ions[a]

Equiv. of metal ion [mol eq.]		$\lambda_{max}^{Abs.b}$ [nm]	$\lambda_{max}^{Flu.b}$ [nm]	$\Phi^{b,c}$ [–]	Stokes shift [nm (cm^{-1})]
	0.0	369	436	0.05	67 (4,164)
Ca^{2+}	1.0×10^5	369	440	0.06	71 (4,373)
Mg^{2+}	2.0×10^5	450	552	0.03	102 (4,106)
Zn^{2+}	1.0×10^5	369	440	0.05	71 (4,373)

[a]The metal-ion source was $Mg(ClO_4)_2$, $Ca(ClO_4)_2$ or $Zn(ClO_4)_2$. [b]Measured for a 4 μmol dm^{-3} sample in CH_2Cl_2–MeCN solution (1: 1 v/v). Excitation at maximum absorption wavelength ($\lambda_{max}^{Abs.}$). [c]Absolute fluorescence quantum yield determined by a calibrated integrating sphere system.

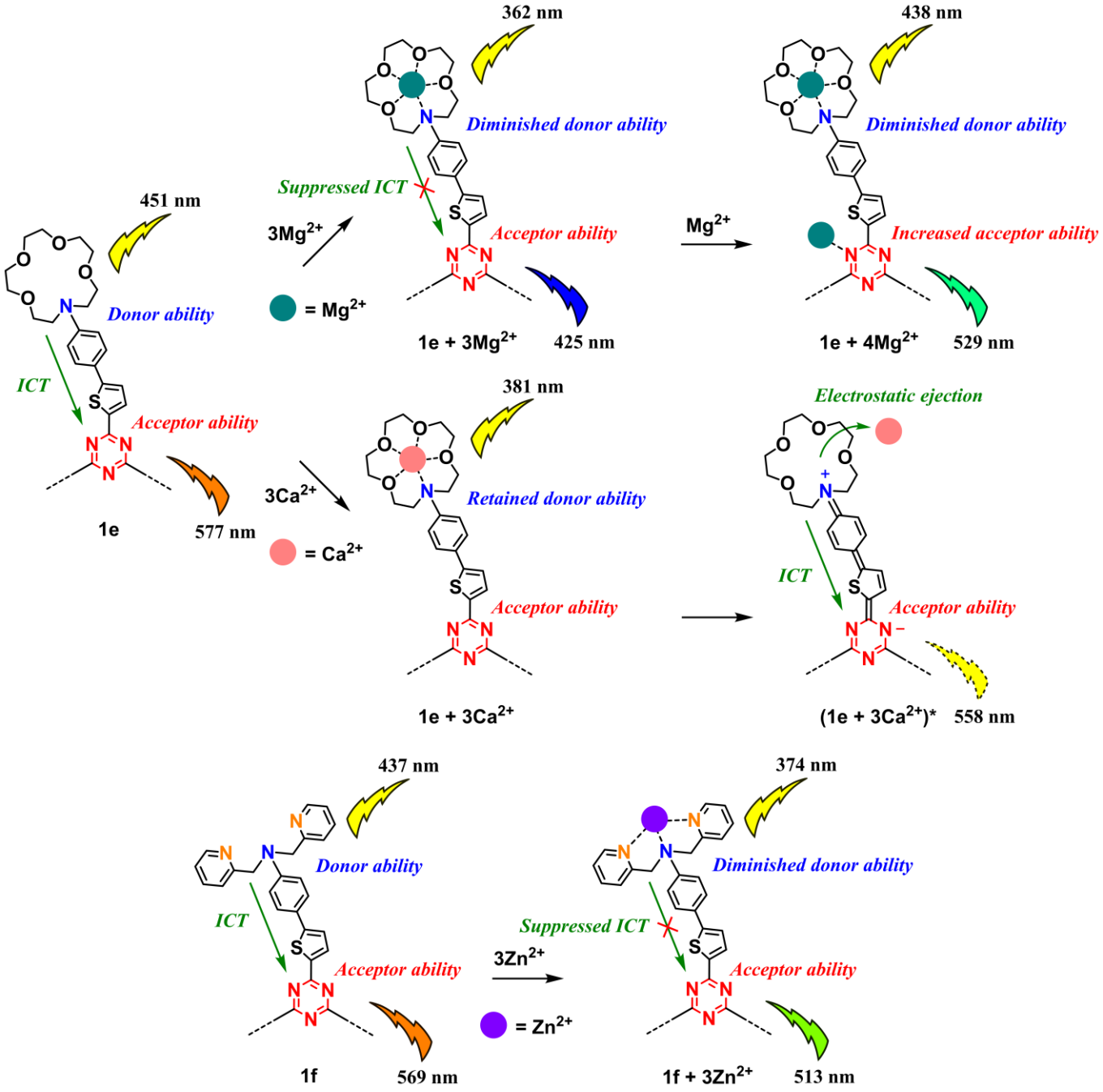

Figure 19. Possible metal-ion-sensing mechanisms of **1e–f**

Figure 19 summarizes the metal-ion binding processes of **1e–f** and their associated optical responses. Compound **1e** with ACE receptors displayed a two- or one-step optical response to Mg^{2+} and Ca^{2+}. The initial binding of Mg^{2+} to the ACE receptors induces blue-shifts in both the absorption and fluorescence bands, enabling the colorimetric and fluorometric detection of Mg^{2+}. The subsequent binding of Mg^{2+} to the 1,3,5-triazine core causes redshifts in the absorption and fluorescence bands, leading to additional colorimetric and fluorometric changes. The binding of Ca^{2+} to the ACE receptors induces a blue-shift of

the absorption band but quenches the fluorescence, enabling the colorimetric and "turn-off" fluorometric detection of Ca^{2+}. Compound **1f** with the DPA receptors displayed a one-step optical response to Zn^{2+}. The binding of Zn^{2+} to the DPA receptors can be exploited for the colorimetric and fluorometric detection of Zn^{2+}, as it induces blue-shifts in both the absorption and fluorescence bands and increases the fluorescence intensity. It was concluded that each compound has a different metal ion-recognition functionality and can be incorporated into a visually detectable metal-ion sensor with sensitivity and selectivity for specific metal ions.

In summary, we showed that by introducing amino-donor-type receptors with different metal-ion binding abilities to **TATTs**, we can induce ICT-based optical responses to different kinds of metal ions. When the metal ions can also bind to the 1,3,5-triazine core, they elicit an additional optical response, resulting in a stepwise color change in both the solution and its emissions. As the **TATTs** are optically responsive to both metal ions and protons, they are expected to realize multi-functional sensors for the visual detection of different cation species.

3. CONCLUSION

This review showcased a series of 2,4,6-tris(5-arylthiophen-2-yl)-1,3,5-triazines (**TATTs**) based on a 2,4,6-tri(thiophen-2-yl)-1,3,5-triazine (**TTT**) skeleton and functionalized with different types of electron-donating aryl groups, yielding a wide variety of star-shaped $(D–\pi)_3–A$ molecules. The **TATTs** with various electron-donating aryl groups (*p*-R–C_6H_4: R = H, ^{n}Bu, ^{n}BuO, ^{n}Bu$_2$N, ACE, or DPA) are endowed with properties and functionalities originating from the geometrically and electronically tunable star-shaped $(D–\pi)_3–A$ structure, including photoabsorption and photoluminescence properties, electrochemical redox reactivities and electrical conductivities, solvatochromic and fluorosolvatochromic sensitivities, and colorimetric and fluorometric cation-sensing functionalities. Most importantly, the **TATTs** can be easily synthesized by changing the coupling partner in the three-fold cross-coupling reaction, which uses 2,4,6-tris(5-bromothiophen-2-yl)-1,3,5-triazine (**TBTT**) as the key intermediate. Moreover, the molecular features of the **TATTs** can be imparted and controlled by selecting electron-donating aryl groups. We therefore suggest that **TATTs** can emerge as research materials with designable molecular structures, synthetic accessibility, diversity and tunability of molecular properties, and potential applicability. We hope that this review will guide the design and construction of new **TATTs** and **TTT**-based star-shaped $(D–\pi)_3–A$ analog molecules with the desired properties and functionalities, thereby helping the development of functional organic materials in the future.

ACKNOWLEDGEMENTS

The original research mentioned in this review resulted from considerable efforts by collaborators and students, and was partly supported by the Japan Society for the Promotion of Science (JSPS) KAKENHI (Grant Number 16K20897). Part of the theoretical results in this review were obtained using the supercomputing resources at the Cyberscience Center, Tohoku University. We sincerely thank all the collaborators and students for their great contributions and also thank all the organizations for their financial and research support.

REFERENCES

1. (a) A. L. Kanibolotsky, I. F. Perepichka, and P. J. Skabara, *Chem. Soc. Rev.*, 2010, **39**, 2695; (b) H. Detert, M. Lehmann, and H. Meier, *Materials*, 2010, **3**, 3218; (c) T. Jarosz, M. Lapkowski, and P. Ledwon, *Macromol. Rapid Commun.*, 2014, **35**, 1006; (d) H. M. Diab, A. M. Abdelmoniem, M. R. Shaaban, I. A. Abdelhamid, and A. H. M. Elwahy, *RSC Adv.*, 2019, **9**, 16606; (e) S. Kotha, M. Meshram, N. R. Panguluri, V. R. Shah, S. Todeti, and M. E. Shirbhate, *Chem. Asian J.*, 2019, **14**, 1356.
2. I. Nenner and G. J. Schulz, *J. Chem. Phys.*, 1975, **62**, 1747.
3. For recent examples see: (a) J. Hu, Y. Li, H. Zhu, S. Qiu, G. He, X. Zhu, and A. Xia, *ChemPhysChem*, 2015, **16**, 2357; (b) T. Matulaitis, N. Kostiv, J. V. Grazulevicius, L. Peciulyte, J. Simokaitiene, V. Jankauskas, B. Luszczynska, and J. Ulanski, *Dyes Pigm.*, 2016, **127**, 45; (c) Y. Wang, W. Liu, J. Deng, G. Xie, Y. Liao, Z. Qu, H. Tan, Y. Liu, and W. Zhu, *Chem. Asian J.*, 2016, **11**, 2555; (d) G. Sathiyan and P. Sakthivel, *Dyes Pigm.*, 2017, **143**, 444; (e) Y. Wang, Y. Jiang, D. Liu, Y. Wang, G. Wang, and J. Hua, *J. Lumin.*, 2017, **190**, 89; (f) T. Matulaitis, P. Imbrasas, N. A. Kukhta, P. Baronas, T. Bučiūnas, D. Banevičius, K. Kazlauskas, J. V. Gražulevičius, and S. Juršėnas, *J. Phys. Chem. C*, 2017, **121**, 23618; (g) I. Marghad, D. H. Kim, X. Tian, F. Mathevet, C. Gosmini, J.-C. Ribierre, and C. Adachi, *ACS Omega*, 2018, **3**, 2254; (h) S. Y. Park, S. Choi, G. E. Park, H. J. Kim, C. Lee, J. S. Moon, S. W. Kim, S. Park, J. H. Kwon, M. J. Cho, and D. H. Choi, *ACS Appl. Mater. Interfaces*, 2018, **10**, 14966; (i) P. Das, A. Kumar, A. Chowdhury, and P. S. Mukherjee, *ACS Omega*, 2018, **3**, 13757; (j) G. Sathiyan, B. Balasubramaniam, S. Ranjan, S. Chatterjee, P. Sen, A. Garg, R. K. Gupta, and A. Singh, *Mater. Today Chem.*, 2019, **12**, 178; (k) B. Liu, H. Wang, and Q. Hu, *Chem. Phys. Lett.*, 2019, **716**, 252; (l) X.-F. Tan, P.-P. Wang, L. Lu, O. Bezvikonnyi, D. Volyniuk, J. V. Grazulevicius, and Q.-H. Zhao, *Dyes Pigm.*, 2020, **173**, 107793.
4. P. Leriche, F. Piron, E. Ripaud, P. Frère, M. Allain, and J. Roncali, *Tetrahedron Lett.*, 2009, **50**, 5673.
5. S. V. Lindeman, V. E. Shklover, Y. T. Struchkov, L. M. Mitina, and V. A. Pankratov, *J. Struct.*

Chem., 1984, **25**, 162.

6. (a) L. Zou, Z. Liu, X. Yan, Y. Liu, Y. Fu, J. Liu, Z. Huang, X. Chen, and J. Qin, *Eur. J. Org. Chem.*, 2009, 5587; (b) T. Yasuda, T. Shimizu, F. Liu, G. Ungar, and T. Kato, *J. Am. Chem. Soc.*, 2011, **133**, 13437; (c) R. Maragani and R. Misra, *Tetrahedron Lett.*, 2013, **54**, 5399; (d) K. Do, H. Choi, K. Lim, H. Jo, J. W. Cho, M. K. Nazeeruddin, and J. Ko, *Chem. Commun.*, 2014, **50**, 10971; (e) W. Huang, H. Wang, L. Sun, B. Li, J. Su, and H. Tian, *J. Mater. Chem. C*, 2014, **2**, 6843; (f) K. Lim, M.-S. Kang, Y. Myung, J.-H. Seo, P. Banerjee, T. J. Marks, and J. Ko, *J. Mater. Chem. A*, 2016, **4**, 1186.
7. (a) H. Muraoka, M. Mori, and S. Ogawa, *Phosphorus, Sulfur Silicon Relat. Elem.*, 2015, **190**, 1382; (b) H. Muraoka, H. Sasaki, and S. Ogawa, *Bull. Chem. Soc. Jpn.*, 2019, **92**, 797; (c) H. Muraoka and S. Ogawa, *J. Synth. Org. Chem. Jpn.*, 2021, **79**, 859.
8. (a) M. M. Heravi, V. Zadsirjan, P. Hajiabbasi, and H. Hamidi, *Monatsh. Chem.*, 2019, **150**, 535; (b) K. Juhász, Á. Magyar, and Z. Hell, *Synthesis*, 2021, **53**, 983.
9. S. Gronowitz and A.-B. Hörnfeldt, 'Thiophenes', Elsevier Academic Press, Oxford, 2004.
10. (a) N. Miyaura, 'Metal-Catalyzed Cross-Coupling Reactions, Second, Completely Revised and Enlarged Edition', Vol. 1, ed. by A. de Meijere and F. Diederich, Wiley-VCH, Weinheim, 2004, pp. 41-123; (b) A. Suzuki, *Angew. Chem. Int. Ed.*, 2011, **50**, 6722.
11. The theoretical calculations were performed using the Gaussian program (Gaussian 09 Revision E.01, M. J. Frisch, G. W. Trucks, H. B. Schlegel, G. E. Scuseria, M. A. Robb, J. R. Cheeseman, G. Scalmani, V. Barone, B. Mennucci, G. A. Petersson, H. Nakatsuji, M. Caricato, X. Li, H. P. Hratchian, A. F. Izmaylov, J. Bloino, G. Zheng, J. L. Sonnenberg, M. Hada, M. Ehara, K. Toyota, R. Fukuda, J. Hasegawa, M. Ishida, T. Nakajima, Y. Honda, O. Kitao, H. Nakai, T. Vreven, J. A. Montgomery, Jr., J. E. Peralta, F. Ogliaro, M. Bearpark, J. J. Heyd, E. Brothers, K. N. Kudin, V. N. Staroverov, T. Keith, R. Kobayashi, J. Normand, K. Raghavachari, A. Rendell, J. C. Burant, S. S. Iyengar, J. Tomasi, M. Cossi, N. Rega, J. M. Millam, M. Klene, J. E. Knox, J. B. Cross, V. Bakken, C. Adamo, J. Jaramillo, R. Gomperts, R. E. Stratmann, O. Yazyev, A. J. Austin, R. Cammi, C. Pomelli, J. W. Ochterski, R. L. Martin, K. Morokuma, V. G. Zakrzewski, G. A. Voth, P. Salvador, J. J. Dannenberg, S. Dapprich, A. D. Daniels, O. Farkas, J. B. Foresman, J. V. Ortiz, J. Cioslowski, and D. J. Fox, Gaussian, Inc., Wallingford CT, 2013). The ground-state geometric optimized structures were obtained using the B3LYP / 3-21G(d) level of theory. Their electronic properties, such as molecular orbital energies and dipole moments, were calculated at the same level of theory. The molecular orbitals of the optimized structures were visualized by the GaussView program (GaussView, Version 6, R. Dennington, T. A. Keith, and J. M. Millam, Semichem Inc., Shawnee Mission, KS, 2016). The excitation energies for the lowest excited states were calculated at the time-dependent (TD)-B3LYP / 6-31G(d,p) or 6-31+G(d) level using the optimized structures.

12. P. Rybczyński, M. H. E. Bousquet, A. K.-Kędziera, B. Jędrzejewska, D. Jacquemin, and B. Ośmiałowski, *Chem. Sci.*, 2022, **13**, 13347.
13. (a) Y. Gong, X. Guo, S. Wang, H. Su, and A. Xia, *J. Phys. Chem. A*, 2007, **111**, 5806; (b) M. Jia, X. Ma, L. Yan, H. Wang, Q. Guo, X. Wang, Y. Wang, X. Zhan, and A. Xia, *J. Phys. Chem. A*, 2010, **114**, 7345.
14. K. M. Omer, S.-Y. Ku, Y.-C. Chen, K.-T. Wong, and A. J. Bard, *J. Am. Chem. Soc.*, 2010, **132**, 10944.
15. J. Pommerehne, H. Vestweber, W. Guss, R. F. Mahrt, H. Bässler, M. Porsch, and J. Daub, *Adv. Mater.*, 1995, **7**, 551.
16. T. Hosokai, H. Muraoka, M. Mori, R. Kurihara, S. Ogawa, and N. Yoshimoto, *Jpn. J. Appl. Phys.*, 2014, **53**, 01AB15.
17. S. Nigam and S. Rutan, *Appl. Spectrosc.*, 2001, **55**, 362A.
18. (a) E. Z. Lippert and Z. Naturforsch, *A: Phys. Sci.*, 1955, **10**, 541; (b) N. Mataga, Y. Kaifu, and M. Koizumi, *Bull. Chem. Soc. Jpn.*, 1956, **29**, 465.
19. B. Dereka, D. Svechkarev, A. Rosspeintner, A. Aster, M. Lunzer, R. Liska, A. M. Mohs, and E. Vauthey, *Nat. Commun.*, 2020, **11**, 1925.
20. (a) A. P. de Silva, H. Q. N. Gunaratne, T. Gunnlaugsson, A. J. M. Huxley, C. P. McCoy, J. T. Rademacher, and T. E. Rice, *Chem. Rev.*, 1997, **97**, 1515; (b) B. Valeur and I. Leray, *Coordin. Chem. Rev.*, 2000, **205**, 3; (c) A. Pal, M. Karmakar, S. R. Bhatta, and A. Thakur, *Coordin. Chem. Rev.*, 2021, **448**, 214167.
21. H. Meier, E. Karpuk, and H. C. Holst, *Eur. J. Org. Chem.*, 2006, 2609.
22. P. Kaur, D. Sareen, M. Kaur, and K. Singh, *Anal. Chim. Acta*, 2013, **778**, 79.
23. E. N. Ushakov, M. V. Alfimov, and S. P. Gromov, *Macroheterocycles*, 2010, **3**, 189.
24. Z. Xu, J. Yoon, and D. R. Spring, *Chem. Soc. Rev.*, 2010, **39**, 1996.
25. D. Vijay and G. N. Sastry, *J. Phys. Chem. A*, 2006, **110**, 10148.
26. M. V. Rusalov, B. M. Uzhinov, M. V. Alfimov, and S. P. Gromov, *Russ. Chem. Rev.*, 2010, **79**, 1099.
27. D. P. Kennedy, C. Gwizdala, and S. C. Burdette, *Org. Lett.*, 2009, **11**, 2587.

Hiroki Muraoka received Ph.D. from Iwate University (Japan) in 2007 under the supervision of Professor Ryu Sato. After working as a project researcher at Iwate University, he joined the research group of Professor Satoshi Ogawa in Iwate University as an assistant professor in 2009, and was promoted to an associate professor in 2020. His current research interests include the design and development of D-π-A molecules with optical and electronic functions.

Satoshi Ogawa started his academic career as a research associate at Tsukuba University in 1990, and received Ph.D. from Tsukuba University in 1991 under the supervision of Professor Naomichi Furukawa. He moved to Iwate University as a research associate in 1992, and was promoted to a lecture, an associate professor, and a full professor in 1993, 1994, and 2006, respectively. His specialized field of research includes the synthesis, characterization, and application of organic main-group compounds. He served as a Vice President/Executive Director of Iwate University, from July 2011 to March 2014, and from March 2015 to March 2020. He has served as a President of Iwate University since April 2020.